Geosci. Model Dev., 14, 7021–7046, 2021
https://doi.org/10.5194/gmd-14-7021-2021
© Author(s) 2021. This work is distributed under
the Creative Commons Attribution 4.0 License.

Geoscientific Model Development
Open Access
EGU

Evaluation of global EMEP MSC-W (rv4.34) WRF (v3.9.1.1) model surface concentrations and wet deposition of reactive N and S with measurements

Yao Ge[1,2], Mathew R. Heal[1], David S. Stevenson[3], Peter Wind[4], and Massimo Vieno[2]

[1]School of Chemistry, University of Edinburgh, Joseph Black Building, David Brewster Road, Edinburgh, EH9 3FJ, UK
[2]UK Centre for Ecology & Hydrology, Bush Estate, Penicuik, Midlothian, EH26 0QB, UK
[3]School of GeoSciences, University of Edinburgh, Crew Building, Alexander Crum Brown Road, Edinburgh, EH9 3FF, UK
[4]The Norwegian Meteorological Institute, Henrik Mohns Plass 1, 0313, Oslo, Norway

Correspondence: Yao Ge (y.ge-7@sms.ed.ac.uk) and Mathew R. Heal (m.heal@ed.ac.uk)

Received: 21 May 2021 – Discussion started: 29 June 2021
Revised: 22 September 2021 – Accepted: 12 October 2021 – Published: 18 November 2021

Abstract. Atmospheric pollution has many profound effects on human health, ecosystems, and the climate. Of concern are high concentrations and deposition of reactive nitrogen (N_r) species, especially of reduced N (gaseous NH_3, particulate NH_4^+). Atmospheric chemistry and transport models (ACTMs) are crucial to understanding sources and impacts of N_r chemistry and its potential mitigation. Here we undertake the first evaluation of the global version of the EMEP MSC-W ACTM driven by WRF meteorology ($1° \times 1°$ resolution), with a focus on surface concentrations and wet deposition of N and S species relevant to investigation of atmospheric N_r and secondary inorganic aerosol (SIA). The model–measurement comparison is conducted both spatially and temporally, covering 10 monitoring networks worldwide. Model simulations for 2010 compared use of both HTAP and $ECLIPSE_E$ (ECLIPSE annual total with EDGAR monthly profile) emissions inventories; those for 2015 used $ECLIPSE_E$ only. Simulations of primary pollutants are somewhat sensitive to the choice of inventory in places where regional differences in primary emissions between the two inventories are apparent (e.g. China) but are much less sensitive for secondary components. For example, the difference in modelled global annual mean surface NH_3 concentration using the two 2010 inventories is 18 % (HTAP: $0.26\,\mu g\,m^{-3}$; $ECLIPSE_E$: $0.31\,\mu g\,m^{-3}$) but is only 3.5 % for NH_4^+ (HTAP: $0.316\,\mu g\,m^{-3}$; $ECLIPSE_E$: $0.305\,\mu g\,m^{-3}$). Comparisons of 2010 and 2015 surface concentrations between the model and measurements demonstrate that the model captures the overall spatial and seasonal variations well for the major inorganic pollutants NH_3, NO_2, SO_2, HNO_3, NH_4^+, NO_3^-, and SO_4^{2-} and their wet deposition in East Asia, Southeast Asia, Europe, and North America. The model shows better correlations with annual average measurements for networks in Southeast Asia (mean R for seven species: $\overline{R_7} = 0.73$), Europe ($\overline{R_7} = 0.67$), and North America ($\overline{R_7} = 0.63$) than in East Asia ($\overline{R_5} = 0.35$) (data for 2015), which suggests potential issues with the measurements in the latter network. Temporally, both model and measurements agree on higher NH_3 concentrations in spring and summer and lower concentrations in winter. The model slightly underestimates annual total precipitation measurements (by 13 %–45 %) but agrees well with the spatial variations in precipitation in all four world regions (0.65–0.94 R range). High correlations between measured and modelled NH_4^+ precipitation concentrations are also observed in all regions except East Asia. For annual total wet deposition of reduced N, the greatest consistency is in North America (0.75–0.82 R range), followed by Southeast Asia ($R = 0.68$) and Europe ($R = 0.61$). Model–measurement bias varies between species in different networks; for example, bias for NH_4^+ and NO_3^- is largest in Europe and North America and smallest in East Asia and Southeast Asia. The greater uniformity in spatial correlations than in biases suggests that the major driver of model–measurement discrepancies (aside from differing spatial representativeness and uncertainties and biases in measurements) are shortcomings in absolute emissions rather than in modelling the atmospheric processes. The comprehensive evaluations presented in this

study support the application of this model framework for global analysis of current and potential future budgets and deposition of N_r and SIA.

1 Introduction

In view of increasing growth in global anthropogenic emissions, the physical and chemical behaviour of reactive nitrogen (N_r) species, especially those that contain reduced N (i.e. gaseous NH_3 and particulate NH_4^+) have been explored in both experimental and modelling studies (Liu et al., 2019; Wagner et al., 2020; Ciarelli et al., 2019; Tang et al., 2021). As the predominant alkaline gas, NH_3 exerts significant control on the formation of ambient particles and the acidity of deposition. It readily reacts with H_2SO_4 and HNO_3 (respectively derived from emissions of SO_2 and NO_x), and the ammonium sulfate ($(NH_4)_2SO_4$) and nitrate (NH_4NO_3) particles formed in these reactions are important in Earth's radiation budget (Laskin et al., 2015) due to their capacity to act as cloud condensation nuclei and to absorb/scatter solar radiation. Crucially, the $(NH_4)_2SO_4$ and NH_4NO_3 secondary inorganic aerosols (SIAs) typically constitute at least a third of the fine particulate matter ($PM_{2.5}$) surface concentration (Li et al., 2017), exposure to which causes substantial premature mortality globally (Burnett et al., 2018). For half the world's population, the $PM_{2.5}$ air pollution burden is increasing (Shaddick et al., 2020). In addition, NH_3 and NH_4^+ enter aquatic and terrestrial ecosystems through wet and dry deposition, where they are powerful nutrients for many plants and microorganisms. As a result, excessive anthropogenic reduced N emissions to the atmosphere can lead to severe eutrophication and formation of hypoxic zones, with their consequent threats to ecosystem diversity (Erisman et al., 2005).

The surface concentrations and deposition fluxes of atmospheric pollutants are influenced by many spatial and temporal factors such as emissions, meteorology, long-distance transport, and chemical transformations. Ambient measurements play a vital role in assessing existing concentrations but can generally only represent the air quality in the local area and cannot immediately distinguish between the influence of local and remote sources. Speciated gas- and particle-phase sampling and analysis is challenging and expensive (Tang et al., 2018b). Consequently, measurements are generally sparsely located and often not very well temporally resolved, even in regions of the world with well-developed air pollution monitoring networks (Tang et al., 2021), which again limits the interpretation of atmospheric chemical and meteorological processes. Moreover, different world regions have monitoring networks that are subject to different analytical and data handling protocols, potentially leading to systematic differences. Non-identical sampling duration and frequencies within these networks also add uncertainties and complexities to global comparison studies.

Compared with measurements, global- and regional-scale atmospheric chemistry transport models such as EMEP MSC-W (Simpson et al., 2012), CMAQ (Byun and Schere, 2006), and WRF-Chem (Chapman et al., 2009) can provide comprehensive simulations of air pollutant concentrations and depositions with greater spatial and temporal resolution and coverage. These models also facilitate insight into the chemical and meteorological linkages between diverse emission sources and the concentration and deposition of pollutants at locations away from initial emissions. Such models are essential when it comes to simulating the impacts of possible future policy actions. A number of global models have already been utilized to investigate sulfate, nitrate, or ammonia budgets, including GISS II-prime (Adams et al., 1999), GEOS-Chem (Pye et al., 2009), LMDz-INCA (Hauglustaine et al., 2014), STOCHEM-CRI (Khan et al., 2020), and multi-model ensemble analysis (Tan et al., 2018). Bian et al. (2017) presented a budget analysis of global nitrate simulations from nine models and found wide variation in the tropospheric burdens of HNO_3, NO_3^-, NH_3, and NH_4^+ between the models. However, global simulations and evaluation of N_r species in atmospheric chemistry transport models remain rare. In particular, there has been little comparison between modelled surface concentrations and wet deposition of N_r species, especially NH_3 and NH_4^+, with regional ground-based measurement networks worldwide, which is the motivation for this work.

Here, we present for the first time a detailed evaluation of the global simulation performance of the EMEP MSC-W chemical transport model coupled with the WRF numerical weather model. Our aim was to compare model output temporally and spatially with available ambient measurements from nine monitoring networks in four global regions. A further aim was to examine the sensitivities of the model–measurement comparison to two different global emission inventories (HTAP v2 and ECLIPSE). The primary focus of the comparisons was on atmospheric concentrations and wet depositions of the N_r and SIA species. We also undertook evaluations for two meteorological years: 2010 and 2015.

2 Methods

2.1 Model description and set-up

The EMEP MSC-W atmospheric chemistry transport model has been developed by the European Monitoring and Evaluation Programme Meteorological Synthesizing Centre – West. As described by Simpson et al. (2012) and at https://www.emep.int (last access: 20 May 2021), EMEP MSC-W is an open-source Eulerian grid model used for applications ranging from scientific research to policy development (Bergström et al., 2014; Mills et al., 2018; Karl et al., 2019; Ciarelli et al., 2019; Jonson et al., 2017; McFiggans et al., 2019). The model uses 21 terrain-following vertical

layers, with the pressure ranging from around 1000 hPa (surface level) to 100 hPa (highest level). We use a lowest layer of ~ 45 m height. Output surface concentrations for major species are adjusted to be equivalent to 3 m above the surface as described in Simpson et al. (2012).

In this study, we utilize the most recent EMEP MSC-W model version rv4.34. Simpson et al. (2020) provide an overview of the changes made to the model since the version rv4.0 documented in Simpson et al. (2012). These changes include improved calculations of aerosol surface area and gas aerosol uptake (Stadtler et al., 2018); additional land cover classes and improved leaf area calculations for global biogenic volatile organic compound (BVOC) emission calculation (Simpson, 2017); a new radiation scheme (Weiss and Norman, 1985) for BVOC and deposition calculations; new chemical mechanisms (Bergström, 2021); and changes related to sea salt, dust, and other emissions handling.

Most studies using EMEP MSC-W utilize meteorological data from the Integrated Forecast System model (IFS) of the European Centre for Medium-Range Weather Forecasts (ECMWF) (Fagerli et al., 2019; Pommier et al., 2020; Simpson et al., 2012). Evaluations of the MSC-W model run with IFS meteorology can be found in Mills et al. (2018), who found good agreement of modelled versus measured O_3 metrics across the Global Atmosphere Watch network; McFiggans et al. (2019), who found good to reasonable agreement of organic aerosol data for European and North American networks; and Bian et al. (2017), who found reasonable agreement for inorganic S and N compounds in a multimodel study.

In contrast, the meteorology used for the EMEP MSC-W model simulations in this study was derived from the Weather Research and Forecast model (WRF, http://www.wrf-model.org, last access: 20 May 2021) version 3.9.1.1 (Skamarock, 2008) at grid resolution of $1^\circ \times 1^\circ$. The WRF model included data assimilation (Newtonian nudging) of the numerical weather prediction model meteorological reanalysis from the US National Center for Environmental Prediction (NCEP)/National Center for Atmospheric Research (NCAR) Global Forecast System (GFS) at 1° resolution every 6 h (Saha et al., 2010). This work uses the Yonsei University (YSU) planetary boundary layer (PBL) scheme. The bulk microphysical parameterization (BMP) scheme is from Lin et at. (2011). The cumulus parameterization uses the Kain–Fritsch scheme. The longwave and shortwave radiation scheme utilizes RRTM/Dudhia. The WRF simulations used the Noah Land Surface Model, for land cover set-up WRF uses the MODIS-derived land cover, and the EMEP MSC-W model uses land data from GLC2000 with the Community Land Model (CLM). The EMEP MSC-W model calculates roughness length and depositions from its own land cover. A higher-resolution UK and Europe regional version of the EMEP-WRF modelling system has previously been evaluated well against field measurements (Vieno et al., 2010, 2014, 2016). However, an assessment of the global version has not yet been undertaken. Moreover, integrating WRF with the EMEP MSC-W model is still an innovative application, as most studies utilize meteorological data from the IFS model as described above.

Two global emission inventories were used in this work. The ECLIPSE (Evaluating the CLimate and Air Quality ImPacts of Short-livEd Pollutant) inventory version V6 (https://iiasa.ac.at/web/home/research/researchPrograms/air/ECLIPSEv6b.html, last access: 20 May 2021) contains annual gridded emissions of SO_2, NO_2, NH_3, CO, CH_4, NMVOCs (non-methane volatile organic compounds), primary fine particulate matter ($PM_{2.5}$), and primary coarse particulate matter (PM_{co}) (Klimont et al., 2017) at $0.5^\circ \times 0.5^\circ$ spatial resolution. Its emission sectors include energy, industry, solvent use, transport, domestic combustion, agriculture, open burning of agricultural waste, and waste treatment. We used ECLIPSE emission inventories for 2010 and 2015 to permit comparison between model and measurements for two self-consistent years of emissions, meteorology, and measurements. The HTAP (Task Force on Hemispheric Transport of Air Pollution) inventory version V2 (https://edgar.jrc.ec.europa.eu/dataset_htap_v2, last access: 20 May 2021) consists of $0.1^\circ \times 0.1^\circ$ gridded monthly emissions of SO_2, NO_2, NH_3, CO, CH_4, NMVOCs, $PM_{2.5}$, PM_{10}, black carbon (BC), and organic carbon (OC) for 2010 (2015 was not available at the time of this work) from seven sectors (international and domestic air, shipping, energy, industry, transport, residential, and agriculture) and was used to investigate the sensitivity of model outputs to different global inventories. The HTAP inventory utilizes nationally reported emissions together with regional scientific inventories (e.g. from the U.S. EPA, the MICS-Asia group, EMEP/TNO, the REAS, and the EDGAR group) for those regions where national emissions are not available (Janssens-Maenhout et al., 2015; Gusev et al., 2012; West et al., 2010).

Both inventories were aggregated to $1^\circ \times 1^\circ$ resolution internally in the model. All inventory emission sector layers were re-assigned to 11 selected nomenclature for sources of air pollution (SNAP) sectors: (1) combustion in energy and transformation industries, (2) non-industrial combustion plants, (3) combustion in manufacturing industry, (4) production processes, (5) extraction and distribution of fossil fuels and geothermal energy, (6) solvent and other product use, (7) road transport, (8) other mobile sources and machinery, (9) waste treatment and disposal, (10) agriculture, and (11) other sources and sinks.

In addition, monthly emission time series by sector and country derived from EDGAR (Emission Database for Global Atmospheric Research, v4.3.2 datasets) temporal emission profiles (Crippa et al., 2020) (https://edgar.jrc.ec.europa.eu/dataset_temp_profile, last access: 20 May 2021) were applied to the ECLIPSE annual total emissions for all pollutants. Therefore, from here on we refer to the inventory with ECLIPSE annual emissions and EDGAR monthly

temporal profiles as ECLIPSE$_E$. All EDGAR emission subsectors ($\sim$ 33) are further divided into 11 SNAP sectors. The time-splitting factor (T_{SNAP}) for a given pollutant for a given country or region was computed as follows. Annual average emission of pollutant from EDGAR v4.3.2 subsector j, $\overline{P}_j$, was calculated as follows:

$$\overline{P}_j = \frac{\sum_{i=1}^{12} P_{ij}}{12}.$$

Monthly time-splitting factor of pollutant from subsector j, T_{E_j}, was calculated as follows:

$$T_{E\_j} = \frac{P_{ij}}{\overline{P}_j}.$$

The weight of T_{E_j} in month i was calculated as follows:

$$W_{ij} = \frac{P_{ij}}{\sum_{j=1}^{n} P_{ij}}.$$

The time-splitting factor for the EMEP MSC-W model SNAP sector in month i was calculated as follows:

$$T_{SNAP} = \frac{\sum_{j=1}^{n} T_{E\_j} \times W_{ij}}{\sum_{j=1}^{n} W_{ij}}.$$

The EMEP MSC-W model default hour-of-day temporal profiles (which varies with SNAP sector) were applied to all countries. The default day-of-week temporal profile was applied to Europe only as neither of the emission inventories supply such temporal information.

Forest and vegetation fire emissions and international shipping emissions are also included in both inventories. Emissions of dimethyl sulfide (DMS), lightning NO_x, soil NO_x and isoprene are set as reported in Simpson et al. (2017, 2020), as are the wind-derived emissions of dust and sea salt (Simpson et al., 2012; Tsyro et al., 2011).

2.2 Measurement datasets

Ambient measurement data were compiled from the 10 regional and national monitoring networks in East Asia, Southeast Asia, Europe, and North America listed in Table 1. The number of monitoring sites in each network varies with year and with species, but Fig. 1 shows the monitoring sites for NH_4^+ in 2015 as an example. The frequency and duration (i.e. averaging) of sampling, and the sampling and analytical methods used, including the size fraction of PM sampled, vary across the measurement networks. Some measurement locations are also deliberately sited to be close to particular industrial or agricultural sources, in which case a model grid average concentration may not reflect the measurement. Although much of this information is presented in official network reports, much useful metadata is absent from the data portals and addition of this information directly to the portals is a recommendation for improvement. In this work, only measurement data with at least 75 % data capture in the year are used to avoid bias. A full data mining of global measurement data was not undertaken here, but we believe we have captured the major networks of long-running, multi-species SIA gas and particle composition and wet deposition measurements.

The Chinese national nitrogen deposition monitoring network (NNDMN) was established in 2010 to measure inorganic N concentrations and deposition fluxes. The first database, NNDMN 1.0, which compiles monthly air concentration and deposition data for NH_3, NO_2, HNO_3, NH_4^+, and NO_3^- up to 2015 was released in May 2019 (Xu et al., 2019).

The acid deposition monitoring network in East Asia and Southeast Asia (EANET) involves 13 countries and provides annual and monthly concentration and acid deposition data for more than 10 species.

The UK Acid Gases and Aerosol Monitoring Network (AGANet, 30 sites) provides long-term national and monthly speciated measurements of acid gases (HNO_3, SO_2, HCl) and aerosol components (NO_3^-, SO_4^{2-}, Cl^-, Na^+, Ca^{2+}, Mg^{2+}) (Tang et al., 2018b). The UK National Ammonia Monitoring Network (NAMN, 95 sites) includes both AGANet and additional sites with monthly measurements of NH_3 and NH_4^+ (Tang et al., 2018a). Both NAMN and AGANet provide monthly average concentrations.

The European Monitoring and Evaluation Programme/Chemical Coordinating Centre (EMEP/CCC) is a collaborative programme for measuring air pollutants across Europe (Tørseth et al., 2012). The measurement frequency varies from hourly and daily to weekly and biweekly or intermittently, such as every 6 d. It also varies between species. This makes it difficult to derive consistent annual and monthly averages comparisons between measurement and model.

The air data of the United States Environmental Protection Agency (EPA) provides access to annual outdoor air quality data including SO_2, NO_2, NH_4^+, NO_3^-, and SO_4^{2-}, collected from state, local, and tribal monitoring agencies across the United States. The Ammonia Monitoring Network (AMoN) and National Trends Network (NTN) are two further US networks, which provide long-term records of weekly or biweekly NH_3 gas concentrations and annual precipitation chemistries, respectively.

In Canada, the National Air Pollution Surveillance (NAPS) program is the main source of ambient air quality data and consists of continuous and time-integrated monitoring of several species. Continuous measurements are implemented for CO, NO_2, NO, NO_x, O_3, SO_2, $PM_{2.5}$, and PM_{10} at hourly resolution. The time-integrated samples collect once per 6 d for a 24 h period, encompass fine ($PM_{2.5}$) and coarse ($PM_{2.5–10}$) aerosol components (e.g. inorganic ions, metals), semi-volatile organic compounds, and volatile organic compounds (VOCs). The Canadian Air and Precipitation Monitoring Network (CAPMoN) is designed to study the regional patterns and trends of atmospheric pollutants,

Table 1. Summary of surface monitoring networks used in the model–measurement comparisons. The last access date for all URLs cited in this table is 20 May 2021.

Region	Network	Source
East and Southeast Asia	NNDMN (China)	https://www.nature.com/articles/s41597-019-0061-2
	EANET	https://www.eanet.asia
Europe	AGANet (UK)	https://uk-air.defra.gov.uk/networks/network-info?view=aganet
	NAMN (UK)	https://uk-air.defra.gov.uk/networks/network-info?view=nh3
	EMEP/CCC	http://ebas-data.nilu.no/default.aspx
North America	NAPS (Canada)	https://www.canada.ca/en/services/environment/weather/airquality.html
	CAPMoN (Canada)	https://www.canada.ca/en/environment-climate-change/services/air-pollution/monitoring-networks-data/canadian-air-precipitation.html
	EPA air data (US)	https://www.epa.gov/outdoor-air-quality-data
	AMoN (US)	http://nadp.slh.wisc.edu/data/AMoN/
	NTN (US)	http://nadp.slh.wisc.edu/NTN/

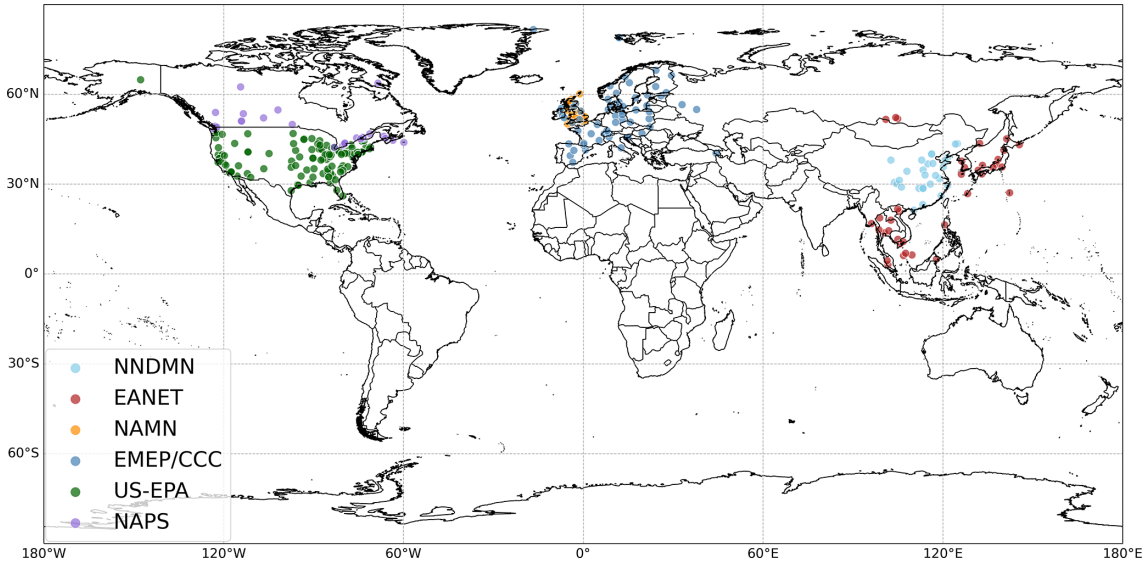

Figure 1. Locations of sites in the six networks that measured particle-phase NH_4^+ in 2015.

such as acid rain, smog, particulate matter, and mercury, in both air and precipitation. Regional precipitation and wet deposition data from CAPMoN were collected through wet precipitation collectors.

The calculations of model–measurement comparison statistics (e.g. Pearson's correlation coefficient, mean bias, mean absolute error) are shown in the Supplement.

3 Results

3.1 Comparison between use of HTAP and ECLIPSE$_E$ emission inventories

3.1.1 Emissions

The global map of 2010 annual NH_3 emissions from ECLIPSE$_E$ is shown in Fig. 2a. Hot spots of NH_3 emissions occur across the globe in areas characterized by dense populations and intensive agricultural activities, most notably in the Indo-Gangetic Plain in India and the North China Plain but also Indonesia, Europe, United States, Mex-

ico, and Brazil. The area-weighted average NH_3 emissions (over the whole global domain) in 2010 are 105 and 121 mg m^{-2} for HTAP and ECLIPSE$_E$, respectively. The individual grid annual NH_3 emission in 2010 varies from 0.00 to 10 692 mg m^{-2} for the HTAP inventory and from 0.00 to 12 244 mg m^{-2} for the ECLIPSE$_E$ inventory. Note that in the following sections all emissions and concentrations are expressed as mass of the species unless otherwise stated, e.g. as μg N m^{-3}.

Figure 2b maps the differences in annual NH_3 emissions between the ECLIPSE$_E$ and HTAP inventories for 2010. Clear differences between the two emission inventories are observed in China, India, and several Southeast Asian countries, but differences in other world regions are relatively small: more than 70 % of the relative differences in ECLIPSE$_E$ HTAP emissions, the majority of which are positive, are within ±10 % of the average inventory emission for that grid. The ECLIPSE$_E$ inventory NH_3 emissions are larger than the HTAP inventory emissions in the northern and southeastern parts of China, the western coastal area of continental Europe, central Africa, Brazil, and Argentina. The largest difference of 6496 mg m^{-2}, which is 73 % of the inventory mean emission of 8956 mg m^{-2} for that model grid, is in eastern China (Fig. 2b). In contrast, HTAP reports larger NH_3 emissions than ECLIPSE$_E$ in areas of Southeast Asia, India, and the western United States. The largest negative difference of −4281 mg m^{-2} (equating to 124 % of the grid mean 3452 mg m^{-2}) is located on the western coast of the United States. Relative NH_3 emission differences that are outside of ±100 % of the average NH_3 emissions from the two inventories for that grid only account for 13 % of the total number of grid cells, and the majority of instances where relative difference is large are for grids that have only low emissions, for which a small absolute difference equates to large relative difference.

Aside from the instances of quite localized discrepancies in the NH_3 emissions between the two inventories, the small median positive (7.90 mg m^{-2}) and negative (−12.0 mg m^{-2}) differences, together with the global area-weighted average difference of only 16.0 mg m^{-2} (14 % relative to the mean emission of the two inventories), indicate that ECLIPSE$_E$ and HTAP provide very similar annual NH_3 emissions in most grids over the whole global domain.

The seasonal profile of spatially averaged monthly NH_3 emissions of the two inventories in 2010 was also investigated for East Asia, Southeast Asia, Europe, and North America separately. The detail is presented in the Supplement. Clear NH_3 emission peaks in spring and summer are observed in both inventories for all four global regions. In general, ECLIPSE$_E$ shows greater monthly variations than HTAP in East Asia, Southeast Asia, and Europe but not North America, which is strongly indicative of different monthly (or day-of-week) temporal factors applied to annual totals in different inventories.

Similar observations derive from comparisons of emissions of NO_x and SO_x in the two inventories (Figs. S1 and S2 in the Supplement). For example, the global area-weighted average difference in annual NO_x emissions between the two inventories is only 11.0 mg m^{-2} (2.9 %), whilst the maximum positive and negative differences for an individual model grid (ECLIPSE$_E$ – HTAP) are 15 389 mg m^{-2} (162 %) and −26 815 mg m^{-2} (−186 %), respectively. These large local differences in NO_x emissions are presumably due to the inclusion or exclusion of a specific point source in one emission inventory but not the other. The shipping emission profiles included in the two inventories are also slightly different. For instance, ECLIPSE$_E$ provides higher NO_x emissions in the Yellow Sea, South China Sea, and Bay of Bengal than HTAP (Fig. S1). Therefore, the differences between the two inventories may not have a large influence on global simulations but may have larger impact on regional modelling at higher spatial resolution.

3.1.2 Reduced N concentrations

Figure 3 presents examples of the global model output: maps of the global distributions of annual mean surface concentrations and total (wet + dry) depositions of reduced N (i.e. $NH_3 + NH_4^+$) in 2010 using the ECLIPSE$_E$ inventory. The largest reduced N concentrations (Fig. 3a) are located in regions of high NH_3 emissions (shown in Fig. 2): notably eastern China, northern India, and Indonesia, followed by northern Italy, Germany, the midwestern United States, and southern Brazil. Reduced N concentrations reach ∼ 35 μg N m^{-3} in parts of China. Annual deposition of reduced N (Fig. 3b) shows clear decreasing gradients from continental regions to surrounding oceans with maxima of 5000–5200 mg N m^{-2} in eastern and southern Asia and 1800–2000 mg N m^{-2} in central Europe and the midwestern and southern United States. These regions are characterized not only by high emissions of reduced N but also large emissions of SO_x and NO_x (Figs. S1 and S2), reflecting the areas of greatest anthropogenic activities. Our spatial patterns of reduced N species are consistent with other global modelling studies (Hauglustaine et al., 2014; Xu and Penner, 2012; Pringle et al., 2010). The model–measurement comparisons we carry out for this study cover the majority of these hot spot regions.

The influences of the two emission inventories on model simulated surface concentration differs according to consideration of the primary or secondary component and varies from one region to another. Globally, the difference in modelled area-weighted annual mean surface NH_3 concentration using the two 2010 inventories is 18 % (HTAP: 0.26 μg m^{-3}; ECLIPSE$_E$: 0.31 μg m^{-3}). The relative difference is the same when considering land-only area-weighted mean surface NH_3 concentration (0.83 and 0.99 μg m^{-3} for HTAP and ECLIPSE$_E$, respectively). In contrast, the difference for global area-weighted mean surface NH_4^+ concentration is only 3.5 % for NH_4^+ (HTAP: 0.316 μg m^{-3};

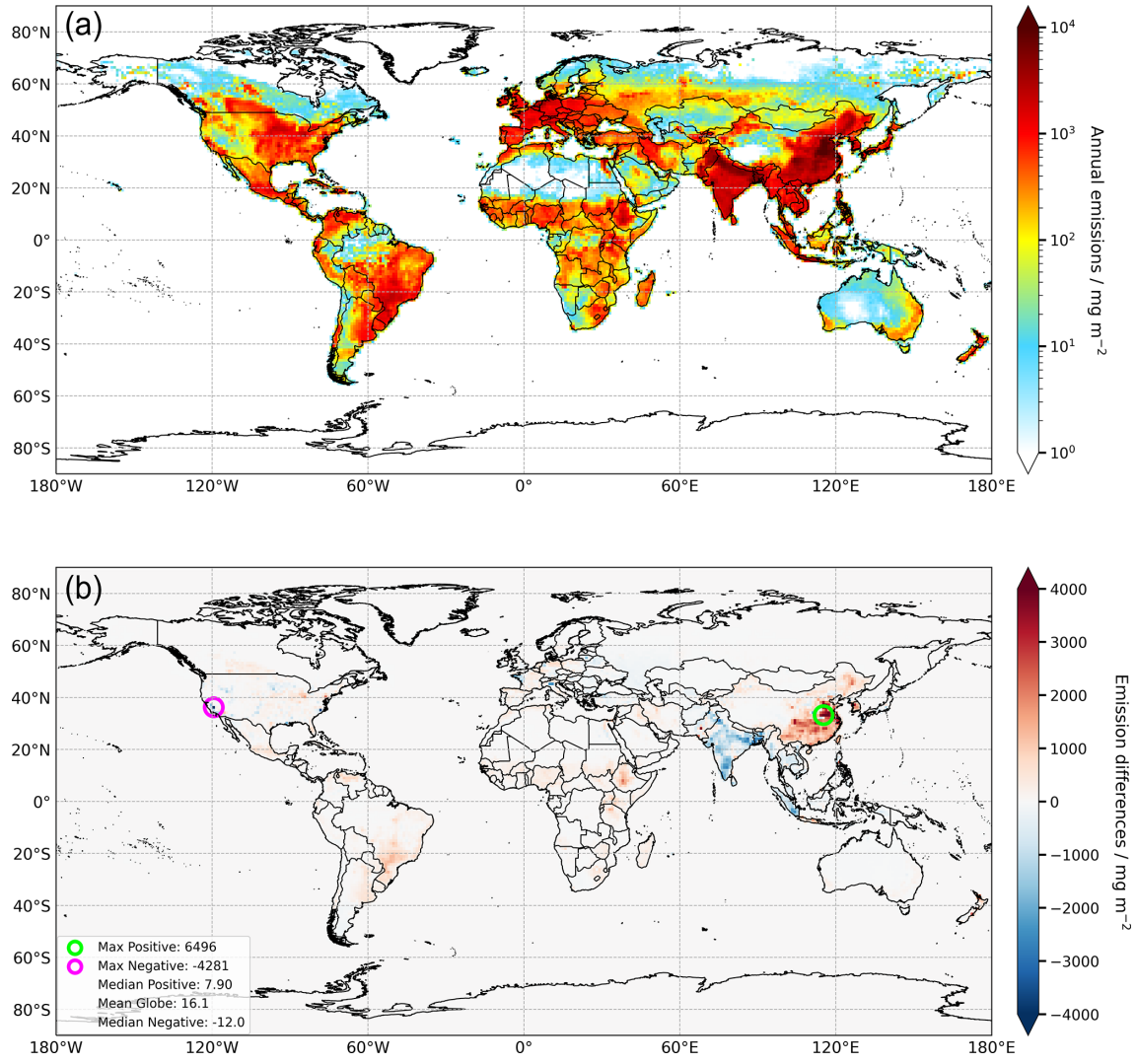

Figure 2. **(a)** Global annual NH_3 emissions for 2010 from $ECLIPSE_E$. **(b)** The difference in 2010 annual NH_3 emissions ($mg\,m^{-2}$) between $ECLIPSE_E$ and HTAP ($ECLIPSE_E$ – HTAP). The inset panel provides the maximum, median, and mean values of both positive and negative differences across individual emission grids.

$ECLIPSE_E$: $0.305\,\mu g\,m^{-3}$) or 5.0 % for the land-only area-weighted NH_4^+ concentrations of 0.755 and $0.718\,\mu g\,m^{-3}$, respectively.

For a regional perspective, Figs. 4 and S5 in the Supplement respectively compare the modelled NH_3 and NH_4^+ concentrations using the two emission inventories for the grids in which there are also available measurements from the monitoring networks. Considering all measurement locations globally, the model simulated concentrations using the two inventories are extremely well spatially correlated with each other at $R = 0.95$ for NH_3 and 0.98 for NH_4^+. The average difference in global surface NH_3 concentration between model simulations using $ECLIPSE_E$ and HTAP based on measurement locations is $0.34\,\mu g\,m^{-3}$, which corresponds to only 15 % of the model average concentration of $2.30\,\mu g\,m^{-3}$ using the $ECLIPSE_E$ inventory or 17 % of the model average concentration of $1.96\,\mu g\,m^{-3}$ using the HTAP inventory.

The model concentrations using the two emission inventories are similarly linearly correlated with measurements (Fig. 4). As discussed above, systematic differences between modelled and measured concentrations of NH_3 in East Asia and Southeast Asia can be attributed at least in part to local differences in NH_3 emissions among different inventories. The average modelled NH_3 concentrations in China derived from $ECLIPSE_E$ and HTAP (based on measurement locations) are 12.3 and $7.9\,\mu g\,m^{-3}$, respectively. The systematically greater modelled NH_3 concentrations using $ECLIPSE_E$ compared to HTAP is consistent with the $ECLIPSE_E$ inventory's larger NH_3 emissions over eastern and southern China (Fig. 2), where the majority of the NNDMN measurement sites are located (Fig. 1).

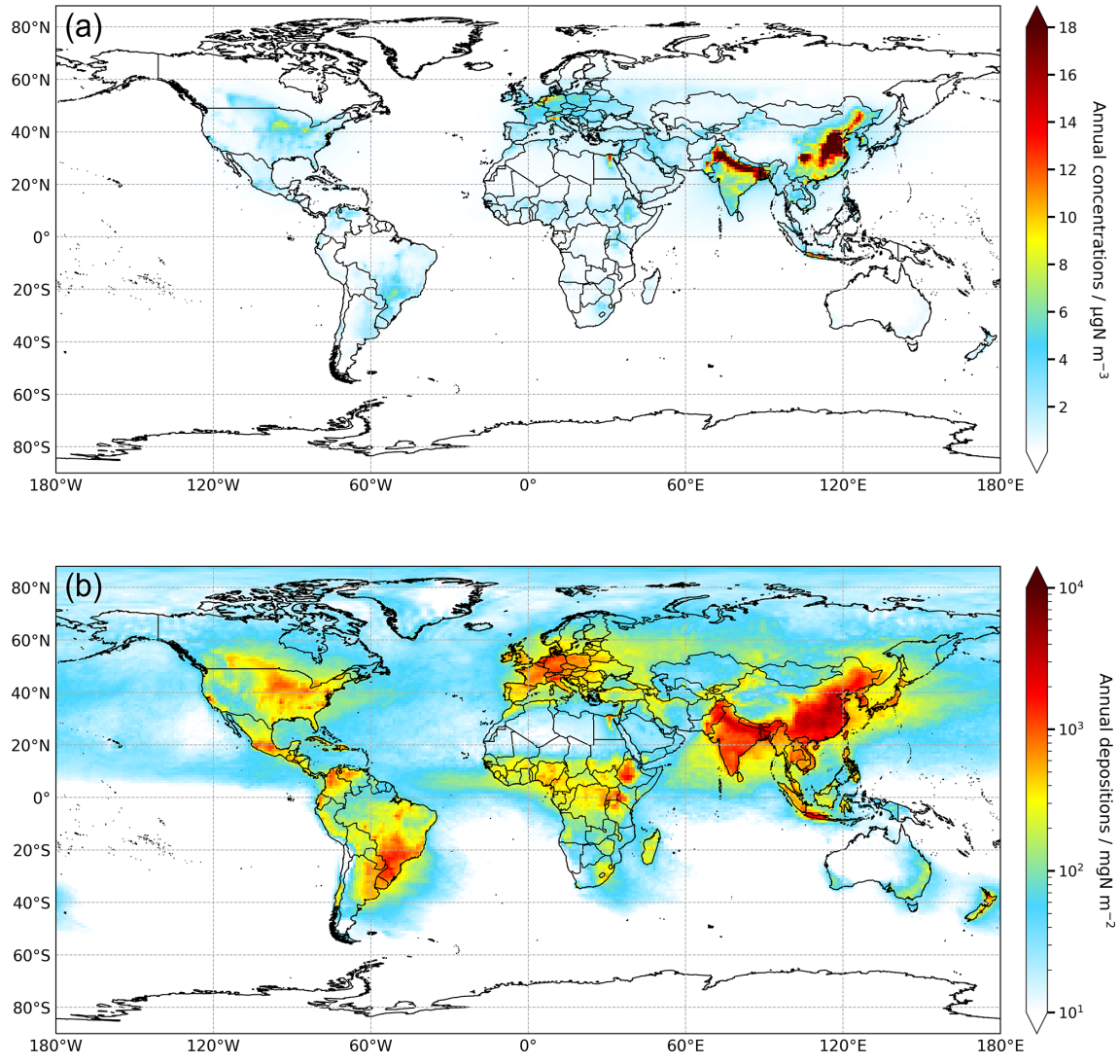

Figure 3. (a) Annual mean surface concentrations and **(b)** annual total (wet + dry) depositions of reduced N ($NH_3 + NH_4^+$) for 2010 based on the ECLIPSE$_E$ inventory.

For measurement locations in Southeast Asia, Fig. 4 shows that modelled NH_3 concentrations are generally lower than their respective measured concentrations for simulations using both emissions inventories. However, as for China, model simulations of NH_3 using the two inventories are spatially well correlated with each other ($R = 0.92$). The overall average modelled NH_3 concentration (based on grids containing EANET sites) of 1.99 μg m^{-3} using the HTAP inventory is slightly greater than the average concentration of 1.50 μg m^{-3} using the ECLIPSE$_E$ inventory. Using the HTAP inventory also gives a slightly larger range in simulated NH_3 concentrations (0.00–9.14 μg m^{-3}) for the grids with measurement sites than the range (0.01–6.54 μg m^{-3}) when using the ECLIPSE$_E$ inventory. This is again consistent with the smaller emissions for ECLIPSE$_E$ in most southeastern Asian countries in 2010 (Fig. 2).

In North America and Europe there are similar linearities between the modelled and measured NH_3 concentrations when using either of the HTAP and ECLIPSE$_E$ inventories (Fig. 4). In general, both inventories produce smaller concentrations than measurements in Europe, with ECLIPSE$_E$ underestimating more, and higher concentrations than measurements in North America, with ECLIPSE$_E$ overestimating more. In other words, the ECLIPSE$_E$ inventory yields smaller NH_3 concentrations in Europe but higher concentrations in North America compared with the HTAP inventory. The differences in NH_3 emissions between the two inventories are very similar in these two regions: Fig. 2 shows that the differences in emissions are generally close to zero and that differences are both positive and negative. Therefore, it is the location of the measurement site that likely influences the model evaluation statistics. The modelled NH_3 concen-

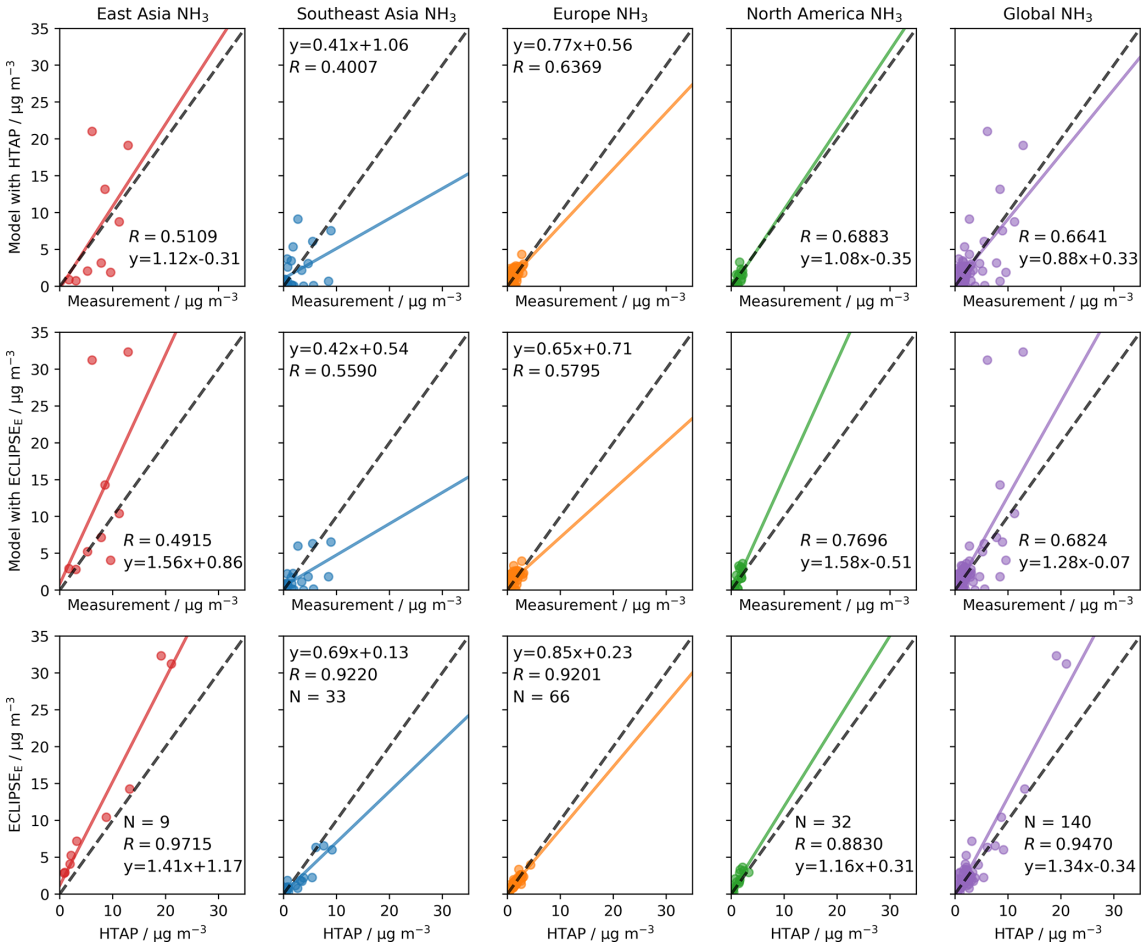

Figure 4. Comparisons of annual average surface concentrations of NH_3 for eight monitoring networks in 2010 – NNDMN from China as East Asia, EANET as Southeast Asia, NAMN and AGANet (UK) and EMEP/CCC plotted together here as Europe, and the EPA and AMoN (USA) and NAPS (Canada) plotted together here as North America – and for all networks combined ("global"). The upper row of plots is modelled versus measured values using the HTAP emission inventory. The middle row is modelled versus measured values using the $ECLIPSE_E$ emission inventory. The lower row is the modelled data for the two inventories plotted against each other for the same set of model grids that contain measurement sites. In each plot, N is the total number of scatter points, R is the Pearson correlation coefficient, the dashed black line is the 1 : 1 line, and the solid coloured line is the trend line corresponding to the equation presented.

trations in North America (based on network locations) are in the ranges 0.01–3.30 and 0.04–3.64 µg m^{-3} for simulations with HTAP and $ECLIPSE_E$ inventories, respectively, while in Europe the equivalent modelled NH_3 concentration ranges are 0.00–4.36 and 0.00–3.95 µg m^{-3}. The average NH_3 concentration difference (based on network locations) in North America between the two emission inventories is 0.47 µg m^{-3} ($ECLIPSE_E$ – HTAP), whilst this difference in Europe is only 0.03 µg m^{-3}.

The impact of emission inventory differences on concentrations of secondary pollutants is much smaller than for primary pollutants since the former are influenced by multiple emissions and the timescales for their formation act to smooth out spatial differentials in primary emissions. This is illustrated by the generally better agreement between model outputs for both the HTAP and $ECLIPSE_E$ emissions inventories and the network measurements of annual NH_4^+ concentrations in Fig. S5 than for NH_3 in Fig. 4. Thus, the correlations between modelled and measured NH_4^+ at all network locations are 0.88 (range 0.54–0.92 for the four separate regions) and 0.90 (0.74–0.90) for simulations using the HTAP and $ECLIPSE_E$ inventories, respectively, whilst the corresponding correlation coefficients for NH_3 are 0.66 (0.40–0.69) and 0.68 (0.49–0.77).

The differences in NH_4^+ concentrations in simulations using the two emission inventories (Fig. S5) are also smaller than for NH_3 (Fig. 4), as shown by concentrations that are closer to 1 : 1 in all regions. For example, whilst modelled NH_3 concentrations in China derived using the $ECLIPSE_E$ inventory are on average 56 % higher than those derived using the HTAP inventory, the NH_4^+ concentrations are very similar. The annual average NH_4^+ concentrations (based on

network locations) in China are 7.30 and 7.15 $\mu g\,m^{-3}$ for HTAP and $ECLIPSE_E$, respectively, which is a difference of only 2 %. More detail is presented in the Supplement.

In summary, whilst there are some spatial differences in annual emissions between the HTAP and $ECLIPSE_E$ inventories, e.g. for NH_3 emissions in China and India, emission differences on a global scale are small. The difference in global average NH_3 emissions (for 2010) is 16.0 $mg\,m^{-2}$ ($ECLIPSE_E$ – HTAP), which is 14 % of the average of the HTAP and $ECLIPSE_E$ global mean NH_3 emissions of 105 and 121 $mg\,m^{-2}$, respectively. The spatial heterogeneity in the positive and negative differences in emissions worldwide indicates no global difference between them. The regional differences in emissions between the two inventories impact differently on modelled surface concentrations of primary and secondary species. Both inventories yield model results that show similar linear correlations with ambient NH_3 and NH_4^+ concentration measurements and similar underestimations and overestimations in different monitoring networks. The seasonality in NH_3 emissions of HTAP and $ECLIPSE_E$ are similar, although the latter projects greater monthly fluctuations in East Asia, Southeast Asia, and Europe, but not North America, which indicates discrepancies in temporal (monthly or day-of-week) factors applied to annual totals in different inventories.

3.1.3 Evaluation of model response to changes between 2010 and 2015 $ECLIPSE_E$ emissions

An evaluation was also undertaken of how the modelled concentrations and depositions respond to the change in emissions in simulations using the 2010 and 2015 $ECLIPSE_E$ emissions data, and of how these responses compared with the changes observed in the measurements between the 2 years. This analysis is presented and discussed in the Supplement. Figures S6–S9 respectively present global maps of the differences between 2010 and 2015 of the NH_3, NO_x and SO_x precursor emissions, the modelled NH_3, NO_2 and SO_2 concentrations, the modelled NH_4^+, NO_3^- and SO_4^{2-} aerosol concentrations, and the modelled total depositions of reduced N, oxidized N and oxidized S. Table S1 in the Supplement quantifies the trends between 2010 and 2015 in the modelled and measured species concentrations for each regional network for those sites where measurement data are available in both 2010 and 2015. The need in this comparison for measurement sites operating in both 2010 and 2015 severely reduces the number of paired comparison data for some measurement networks.

In summary, changes in emissions of NH_3 between 2010 and 2015 $ECLIPSE_E$ inventories are generally small (Fig. S6). The global area-weighted average NH_3 emission increases by 4.5 % from 2010 to 2015. By contrast, NO_x and SO_x emissions show slightly larger variations (Fig. S6). The global area-weighted average emissions of NO_x and SO_x decrease from 2010 to 2015 by 5.7 % and 14 %, respectively. The trends in modelled NH_3, NO_2, and SO_2 annual concentration changes between 2010 and 2015 (Fig. S7 and Table S1) are entirely consistent with the trends in the emissions supplied to the model, and in the corresponding measurements, given both the realistic uncertainties in emissions and measurements (and the small number of measurement data), and the differential influences of meteorology on concentrations between the 2 years. Most parts of the world show increased NH_3 concentrations but decreased NO_2 and SO_2 concentrations from 2010 to 2015. The impacts of emission changes on modelled concentrations of secondary pollutants (Fig. S8 and Table S1), and modelled total deposition of reduced N, oxidized N, and oxidized S (Fig. S9) are varying. The comparison of modelled and measured concentration changes based on measurement locations (Table S1) indicates that trends in modelled and measured concentrations for SO_2 and SO_4^{2-} in most networks from 2010 to 2015 show clear decreases, while for NH_3, NH_4^+, NO_2, HNO_3, and NO_3^- the modelled and measured concentrations reveal a mixture of upward, downward, and no trends but are again generally consistent with each other.

Overall, these comparisons of changes in model-simulated concentration and deposition changes between the 2 years in relation to the changes in measurements (and the emissions) provide useful additional confirmation that the model is behaving in line with expectations, within realistic levels of measurement uncertainty.

3.2 Comparisons of modelled surface concentrations of N_r and SIA species with measurements

Evaluations of modelled versus measured concentrations were undertaken for both 2010 and 2015. The comparisons for the 2 years show similar characteristics. To avoid repetition, the following section presents and discusses the comparisons for 2015, using the $ECLIPSE_E$ inventory, as more measurement data were available for 2015. Throughout this section (and only in this Sect. 3.2) the following notation is used when referring to correlation coefficients. The correlation coefficient applying to all the networks shown in a figure is denoted by R_T (T for total), whilst that for each network individually is denoted by its own subscript: R_N is for NNDMN network; R_E is for EANET network, R_{EM} is for EMEP/CCC network, R_{UK} is for UK network, R_{US} is for US network, and R_{NA} is for NAPS network.

3.2.1 East Asia and Southeast Asia

Figure 5 shows the spatial distribution of modelled and measured 2015 annual average NH_3 concentrations for regions covered by the NNDMN (China) and EANET (East Asia) networks. Scatter plots of the paired model versus measurement annual concentrations for NH_3, NH_4^+, and other gaseous- and particle-phase inorganic components are shown in Fig. 6, illustrating the extent of model–measurement spa-

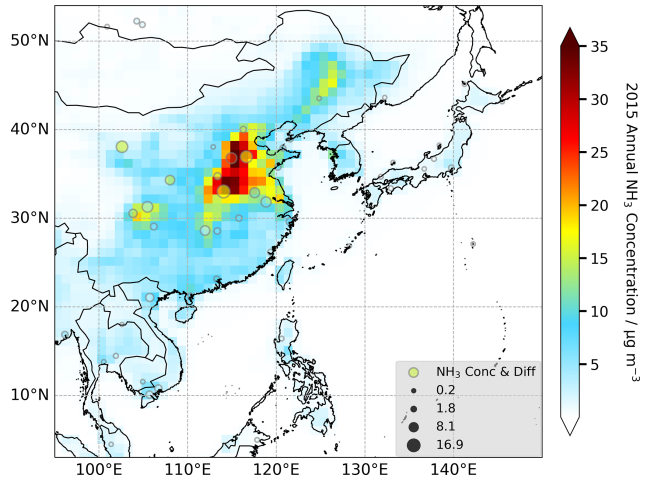

Figure 5. Modelled and measured 2015 annual mean NH_3 concentrations in East Asia and Southeast Asia. Measurements are from the China NNDMN and East Asia EANET networks. Monitoring sites are indicated by circles whose colour represents the measured concentration and whose diameter (see inset legend) represents the absolute difference between model and measurement.

tial correlations. A summary of model evaluation statistics is presented in Table 2.

The model simulates well the overall spatial trend of annual NH_3 concentrations in this region, spanning a range from around 0 to $> 30\,\mu g\,m^{-3}$. Model and measurements consistently show highest NH_3 concentrations in central eastern China (typically $> 15\,\mu g\,m^{-3}$). The observed NH_3 hotspots in North China Plain, Northeast China Plain, and Sichuan Basin are consistent with them being regions of intensive agricultural activities that apply large amounts of fertilizers (Xu et al., 2015). Most areas in other East and South-East Asia countries such as Japan, Thailand, Vietnam and Malaysia have lower NH_3 concentrations (typically $<$ $5\,\mu g\,m^{-3}$) for both model and measurements. Relative differences between model and measurement are generally small for the majority of sampling sites, and where they are large it is a consequence of expressing a difference relative to a small measured concentration. For example, the largest relative difference of 420 %, which is in Vietnam, applies to a very small measured NH_3 concentration of $0.83\,\mu g\,m^{-3}$.

The modelled annual NH_3 concentrations at the NNDMN locations in China are slightly higher than the measurements (NMB = 0.29, Table 2), with 62 % of the sites having positive model minus measurement differences. The sampling site with the largest positive difference is Zhumadian, where modelled NH_3 exceeds the measurement by $16.9\,\mu g\,m^{-3}$ (98 % relative to measurement). The largest negative difference ($-13.0\,\mu g\,m^{-3}$, −82 % relative to measurement) is for the Wuwei site. The large concentration differences reflect the much larger NH_3 concentrations in China. The average difference (mean bias) of annual NH_3 concentrations across all locations in the EANET network is $0.29\,\mu g\,m^{-3}$, which is a factor of 10 smaller than the mean bias of $2.90\,\mu g\,m^{-3}$ for the NNDMN network.

Figure 6 and Table 2 also present the statistical relationships between modelled and measured annual average concentrations in China for NO_2, NH_4^+, HNO_3 and NO_3^-. Both NH_3 and NO_2 display strong linear relationships, while the secondary species NH_4^+ and NO_3^- show poorer correlations. The poorest agreement is for HNO_3 (Table 2). However, modelled HNO_3 concentrations agree much better with measurements in EANET and other networks (shown later), which suggests differences in measurement data among networks. Artefact-free measurement of HNO_3 is a known challenge (Tang et al., 2018b; Cheng et al., 2012; Sickles et al., 1999). The biases between model and NNDMN measurement are quite small for most species except for HNO_3. The overall annual average NH_3 concentrations are 13.0 and $10.1\,\mu g\,m^{-3}$ for model and measurement respectively. The annual modelled network average NO_2 concentration of $28.6\,\mu g\,m^{-3}$ is only 22 % greater than the measured network average NO_2 of $23.5\,\mu g\,m^{-3}$. The modelled and measured network average annual mean NH_4^+ concentrations are equal at $8.1\,\mu g\,m^{-3}$. The proportions of modelled and measured data that are within a factor of 2 are 75 % for NH_3, 83 % for NO_2, 78 % for NH_4^+, and 71 % for NO_3^-; the Fac2 for HNO_3 is, however, only 21 %.

For comparisons at EANET sites, NO_2 has the highest correlation ($R_E = 0.84$) amongst the gaseous species, followed by HNO_3 ($R_E = 0.81$), despite relatively higher biases between model and measurement ($NMB_{HNO_3} = 1.13$, $NMB_{NO_2} = 0.67$). The linear correlations are similar for NH_3 and SO_2, and both also exhibit small biases. The network-averaged modelled and measured annual average NH_3 concentrations are 1.92 and $1.63\,\mu g\,m^{-3}$ respectively (NMB = 0.18). The equivalent data for SO_2 are 3.31 and $2.96\,\mu g\,m^{-3}$ (NMB = 0.12). For the aerosol components, the model simulates higher NH_4^+ concentrations (by 59 %), but slightly lower NO_3^- and SO_4^{2-} concentrations (by 19 % and 11 %, respectively). Linear correlations of aerosol components between model and EANET measurements are high ($R_E = 0.73$–0.74). In summary, the model shows good performance in capturing spatial variations of key inorganic pollutants at EANET locations. The comparison statistics also show an overall better model-measurement linear correlation for EANET than for NNDMN for all species.

3.2.2 Europe

The annual-mean NH_3 concentration map for Europe (Fig. 7) shows the highest NH_3 concentrations ($> 8\,\mu g\,m^{-3}$) are in the Netherlands, Germany and Italy. Concentrations in northern Europe, such as Scandinavia, are smaller ($< 2\,\mu g\,m^{-3}$), which is consistent with less anthropogenic activities and colder temperatures in this region. The model simulations of large NH_3 concentrations in the Po Plain in northern Italy arise from the large NH_3 emissions associated with inten-

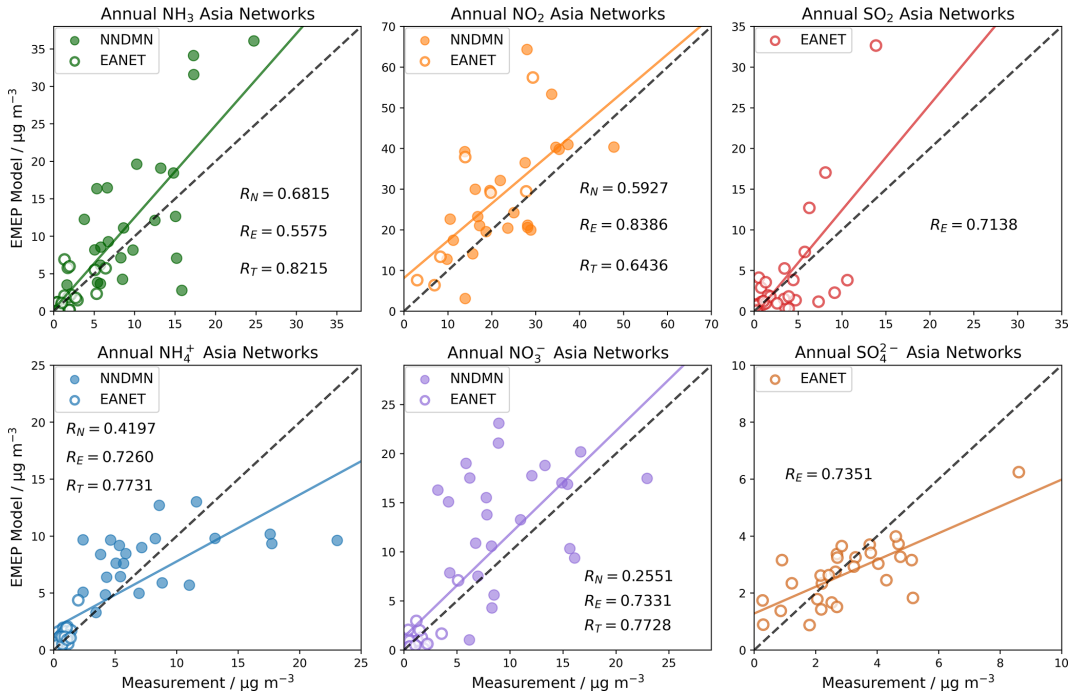

Figure 6. Scatter plots of 2015 annual mean modelled and measured NH_3, NO_2, HNO_3, SO_2, NH_4^+, NO_3^-, and SO_4^{2-} concentrations at East Asian and Southeast Asian monitoring network locations. In each plot, the solid line is the least-squares regression line and the dashed black line is the 1 : 1 line. R_N is for NNDMN network. R_E is for the EANET network. R_T is the overall correlation coefficient between the model and all measurements shown.

Table 2. Summary statistics of model comparison with measurements for 2015 in East Asia and Southeast Asia (NNDMN and EANET networks). N is the number of paired data of model and observation. R_N and R_E are Pearson's coefficients for NNDMN and EANET respectively. Fac2 is the fraction of data points within a factor of 2. Mean_O and Mean_M are annual average concentrations ($\mu g\,m^{-3}$) of observation and model respectively. NMB is normalized mean bias, NME is normalized mean error.

NNDMN	N	R_N	Fac2 fraction	Mean_O	Mean_M	NMB	NME
NH_3	24	0.68	0.75	10.1	13.0	0.29	0.57
NO_2	24	0.59	0.83	23.5	28.6	0.22	0.39
HNO_3	24	−0.18	0.21	4.90	1.93	−0.61	0.64
NH_4^+	23	0.42	0.78	8.10	8.12	0.00	0.46
NO_3^-	24	0.26	0.71	10.0	13.8	0.38	0.62
EANET	N	R_E	Fac2 fraction	Mean_O	Mean_M	NMB	NME
NH_3	27	0.56	0.52	1.63	1.92	0.18	0.69
NO_2	7	0.84	0.71	15.6	25.9	0.67	0.68
HNO_3	28	0.81	0.39	0.63	1.33	1.13	1.19
SO_2	36	0.71	0.44	2.96	3.31	0.12	0.81
NH_4^+	29	0.73	0.62	0.75	1.19	0.59	0.73
NO_3^-	29	0.73	0.38	1.10	0.89	−0.19	0.67
SO_4^{2-}	29	0.74	0.83	3.03	2.71	−0.11	0.31

sive farming of pigs, cattle and poultry (Carozzi et al., 2013; Skjøth et al., 2011). In the UK, NH_3 concentrations generally display a decreasing trend from south to north for both model and measurement although Northern Ireland is a relatively high NH_3 region as well. Most sites with NH_3 concentrations around or below 1 $\mu g\,m^{-3}$ are in northwest Scotland, where modelled NH_3 concentrations are equally low.

Across all monitoring sites in Europe, 79 % show positive differences for model minus measurement of annual NH_3. The monitoring locations with the largest differences (3.11–3.98 $\mu g\,m^{-3}$, Fig. 7) are located in Germany and Switzer-

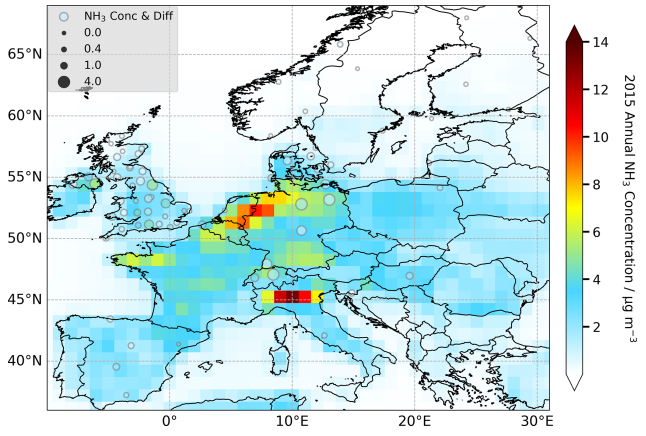

Figure 7. Modelled and measured 2015 annual mean NH_3 concentrations in Europe. Measurements are from the UK NAMN and Europe EMEP/CCC networks. Monitoring sites are indicated by circles whose colour represents the measured concentration and whose diameter (see inset legend) represents the absolute difference between model and measurement.

land, while most sites with differences close to zero are situated in Norway, Sweden, Finland and Scotland. The site with the largest relative difference, Rannoch in the highlands of Scotland, has an extremely low measured concentration of 0.07 $\mu g\,m^{-3}$ relative to the modelled concentration, also low), of 1.13 $\mu g\,m^{-3}$. A number of sites which have negative model minus measurement differences are in southern England and eastern Northern Ireland. The largest model underestimation of NH_3 ($-3.18\,\mu g\,m^{-3}$) is at the Brompton site in England which also has the highest observed NH_3 concentrations for the UK. However, it is important to note that the UK NAMN is a high spatial density NH_3 monitoring network, with many sites deliberately located near local emission sources of NH_3 (Tang et al., 2018a), which the global model grid-average cannot capture.

The linear relationships between model and measurement for 2015 annual average NH_3, NO_2, SO_2, NH_4^+, NO_3^-, and SO_4^{2-} concentrations in Europe are shown in Fig. 8 and a summary of the statistical comparisons is shown in Table 3. A few UK NAMN sites are part of the European EMEP/CCC network. Where a model grid contains multiple measurement sites, the average of the measured values is used.

There is a clear linear correlation between model and measurement for both primary and secondary species (Fig. 8). Correlation is highest for NO_3^- ($R_T = 0.80$), followed by NO_2 and NH_4^+ ($R_T = 0.71$) and weakest for NH_3 ($R_T = 0.51$). However, the NH_3 data appear to be distributed into two groups, one characterized by positive model bias mainly associated with EMEP/CCC network locations and one characterized by negative model bias mainly associated with the UK network. The former may be a result of overestimation of NH_3 in the emission inventory, the latter may be caused by UK measurement locations adjacent to agricultural NH_3 sources (Tang et al., 2018a). The model–measurement comparisons of other gaseous species (NO_2, SO_2, and HNO_3) all show better correlations ($R_T = 0.60$–0.71) and smaller differences (NME 0.50–0.70) in comparison with NH_3.

The modelled concentrations of secondary components, NH_4^+, NO_3^-, and SO_4^{2-}, all match well with the spatial variations of measurements, with R_T varying from 0.69 to 0.80 (Fig. 8). All three components show higher modelled than measured concentrations to a varying degree. The network-averaged NH_4^+ concentrations are 1.11 and 0.56 $\mu g\,m^{-3}$ for model and measurement, respectively. For NO_3^-, the modelled average concentration is 2.18 $\mu g\,m^{-3}$, which is around twice the measurement mean. In comparison with NH_4^+ and NO_3^-, SO_4^{2-} shows a smaller NMB (0.32) and a larger Fac2 fraction (64 %).

In conclusion, across Europe the model exhibits a good performance in simulating annual average concentrations and spatial variations of major inorganic air pollutants, but with an overestimation of secondary NH_4^+, NO_3^-, and SO_4^{2-}. The overall agreement between model outputs and ambient measurements in Europe networks is as good as that in EANET network.

3.2.3 United States and Canada

Modelled and measured 2015 annual average NH_3 concentrations and differences in North America are shown in Fig. 9. The Canadian NAPS network includes limited sampling sites for NH_3, and all of them are situated close to the border with the USA. Areas with the highest NH_3 concentration are located in the midwestern United States according to the model, but there are only a few measurement locations in these regions. Annual average NH_3 measurements in North America vary from 0.39 to 3.74 $\mu g\,m^{-3}$, while the model concentrations at those locations range from 0.13 to 4.62 $\mu g\,m^{-3}$. The model generally simulates slightly higher NH_3 concentrations than measurements: 67 % of the model–measurement differences are positive and the mean model bias is 0.48 $\mu g\,m^{-3}$. The modelled and measured concentrations of NH_3 in North America are comparable to those in Europe and much smaller than those in East Asia.

Figure 10 shows the linear relationships between model and measurement for 2015 annual average NH_3, NO_2, SO_2, NH_4^+, NO_3^-, and SO_4^{2-} in North America. Table 4 provides the summary of statistical comparison metrics. The number of monitoring locations is greater than for the networks in East Asia, Southeast Asia, and Europe. The correlations between modelled and measured annual average NH_3, NO_2, HNO_3 concentrations in North America ($R_T = 0.59$–0.72) are similar to those in Europe and Southeast Asia, but the correlation for SO_2 is poor ($R_T = 0.27$). The reason for the poorer correlation between modelled and measured SO_2 is unknown but may have a few causes: the emission inventory for SO_2 in North America may be too low or some sampling sites may be set close to SO_2 point sources whilst grid-

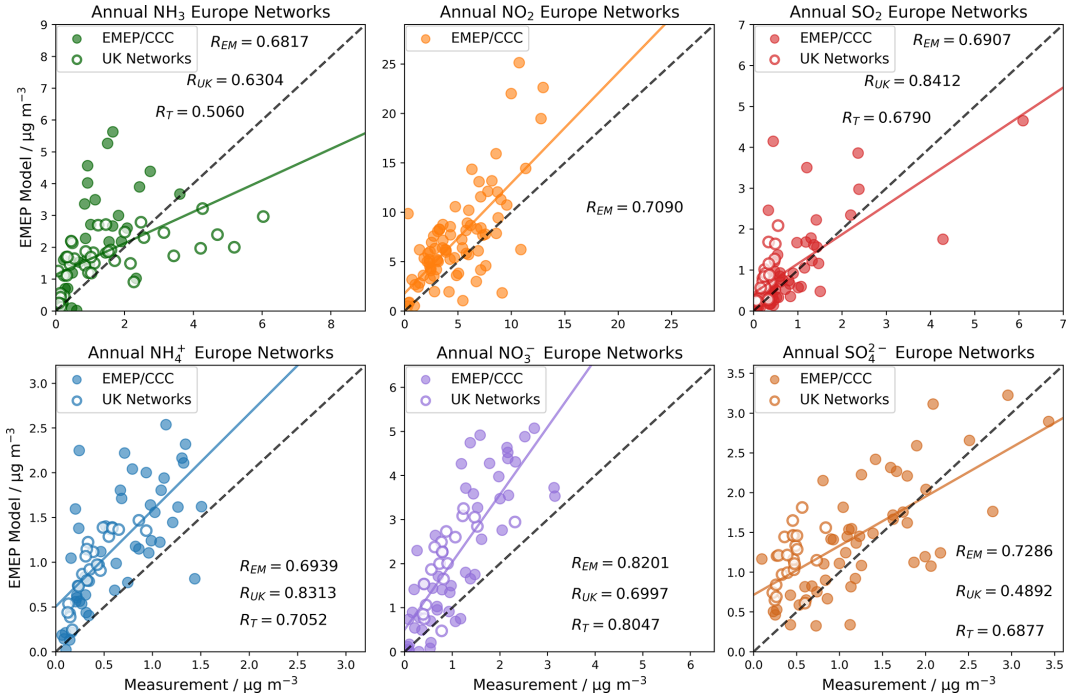

Figure 8. Scatter plots of 2015 annual mean modelled and measured NH_3, NO_2, HNO_3, SO_2, NH_4^+, NO_3^-, and SO_4^{2-} concentrations at European monitoring network locations. In each plot, the solid line is the least-squares regression line and the black dashed line is the 1 : 1 line. R_{EM} is for EMEP/CCC network. R_{UK} is for UK networks. R_T is the overall correlation coefficient between model and all measurements shown.

Table 3. Summary statistics of model comparison with European measurements for 2015 (UK and EMEP/CCC networks). N is the number of paired data of models and observations. R_T is Pearson's coefficient for total measurements in EMEP/CCC and UK networks. Fac2 is the fraction of data points within a factor of 2. Mean_O and Mean_M are annual average concentrations ($\mu g\,m^{-3}$) of observation and model, respectively. NMB is normalized mean bias, and NME is normalized mean error.

Species	N	R_T	Fac2 fraction	Mean_O	Mean_M	NMB	NME
NH_3	77	0.51	0.48	1.26	1.76	0.40	0.79
NO_2	82	0.71	0.62	4.90	7.27	0.48	0.65
HNO_3	48	0.60	0.65	0.38	0.31	−0.18	0.50
SO_2	90	0.68	0.57	0.65	0.90	0.39	0.70
NH_4^+	72	0.71	0.39	0.56	1.11	0.98	1.01
NO_3^-	69	0.80	0.42	1.09	2.18	0.99	1.05
SO_4^{2-}	75	0.69	0.65	1.02	1.34	0.32	0.51

averaged model values are much lower. For the other three gaseous species, the biases between model and measurement are in reasonable ranges. The network-averaged modelled NH_3 concentration is $1.76\,\mu g\,m^{-3}$, which is close to the measured average concentration of $1.28\,\mu g\,m^{-3}$. For HNO_3, 78 % of model data are within a factor of 2 of the measurements, and the overall average concentrations are 0.53 and $0.39\,\mu g\,m^{-3}$ for the model and measurements, respectively (Table 4). Compared to NH_3 and HNO_3, the modelled annual NO_2 concentrations are generally smaller than measurements, leading to a negative NMB of −0.39.

Clear linear relationships are observed between modelled and measured annual average concentrations for all three aerosol pollutants (Fig. 10, Table 4), among which SO_4^{2-} has the highest correlation coefficient (0.86), the largest Fac2 (87 %), and the smallest NMB and NME. This reflects excellent capability by the model to capture the spatial variation of SIA constituents. In terms of absolute concentrations, modelled concentrations are on average higher than measured to varying degrees for NH_4^+, NO_3^-, and SO_4^{2-}, as is the case in Europe. This may be due to gas-to-particle conversion process being too fast in the model or sinks of these secondary species being too small. The network-averaged NH_4^+ con-

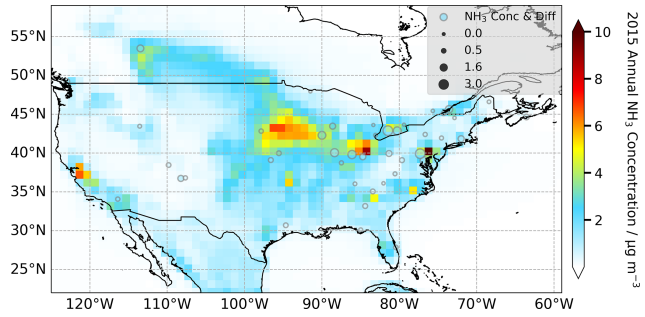

Figure 9. Modelled and measured 2015 annual mean NH_3 concentrations in North America. Measurements are from the US AMoN Network and Canada NAPS Program. Monitoring sites are indicated by circles whose colour represents the measured concentration and whose diameter (see inset legend) represents the absolute difference between model and measurement.

centrations are 1.06 and 0.50 $\mu g\,m^{-3}$ for model and measurement, respectively. For NO_3^- the equivalent concentrations are 1.19 and 0.58 $\mu g\,m^{-3}$. Both NH_4^+ and NO_3^- show relatively small Fac2 fractions due to model overestimation. By contrast, the smallest differences are for SO_4^{2-} concentrations. The average model SO_4^{2-} concentration is 1.27 $\mu g\,m^{-3}$, which only exceeds the average measurement concentration by 31 %.

3.2.4 Comparison of temporal variation of modelled concentrations with measurements

The NNDMN, EANET, NAMN, and EMEP/CCC monitoring networks also provide higher temporal resolution data, which allows a comparative assessment of monthly variations in model simulations (Fig. 11). As well as model-imposed temporal variations in emissions, the NH_3 concentrations are also driven by meteorological variations, in particular warmer temperatures favour partitioning of reduced N to gaseous NH_3. Missing measurement data for certain months and sites means the number of comparisons varies from 1 month to another.

In general, measurements of monthly average NH_3 concentrations in the China NNDMN show a trend of high in summer (mean: 14.6 $\mu g\,m^{-3}$, Table 5) and low in winter (mean: 6.54 $\mu g\,m^{-3}$). The seasonal pattern in the model simulations is slightly different, with dual peaks of NH_3 concentrations in March and August, but seasonal averages for spring and summer in model are similar to summer measurements at 14.6 and 14.8 $\mu g\,m^{-3}$, respectively. Similar to measurements, the modelled NH_3 concentration is also lowest in winter (9.09 $\mu g\,m^{-3}$). For the EANET, both modelled and measured NH_3 median concentrations show a less clear varying trend than other networks, which might be due to the distributions of monitoring sites. A large number of sites in Southeast Asia are located in the tropics where the climate is characterized by a small temperature range and substantial rainfall, which leads to a very small range of fluctuations of NH_3 concentrations. The monthly averages indicate that measurements peak in April and October and are minimum in March and August, while the model has higher concentrations in March, April, August, and October, and lower concentrations in January and February. However, the fluctuation in the all-site monthly averages is small, ranging from 1.21 to 3.21 $\mu g\,m^{-3}$ and from 1.77 to 2.30 $\mu g\,m^{-3}$ for model and measurement, respectively. The variation in monthly medians is even smaller.

For the UK NAMN, both mean and median concentrations (Fig. 11) show that models and measurements exhibit higher NH_3 concentrations in spring and summer, and lower concentrations in winter. One small difference is in the timing of the NH_3 concentration maximum. The highest measured NH_3 concentrations are in spring, whereas modelled concentrations have a maximum in summer. The differences between all-site monthly mean and median concentrations and between the maximum and minimum values in the measurements are much larger than in the model, indicating a broad sub-grid variability that cannot be captured by the global model as the spatial averaging process smooths out these highly localized concentration gradients. For the European EMEP/CCC network, the model is in excellent agreement with measurement in respect to temporal pattern despite its higher absolute concentrations. Both model and measurement show a continuous period of higher NH_3 concentrations from spring to summer and lower NH_3 concentrations in autumn and winter.

Similar model–measurement monthly comparisons for NH_4^+ in 2015 are presented in the Supplement (Fig. S10). Consistent monthly patterns are observed for both model and measurements in the EANET, AGANet (UK), and EMEP/CCC networks: larger NH_4^+ concentrations are found in February, March, and October, while the lowest concentration appears in July. For NNDMN locations, the model and measurement show a similar late summer peak but display an inverse trend in winter and spring.

In summary, the simulated concentrations of NH_3 and NH_4^+ and their month-to-month variability are generally in line with measurement data in most global regions despite the model resolution of $1° \times 1°$. The model comparisons with European measurements exhibit greater agreements than with East Asian and Southeast Asian measurements. The divergence in NNDMN and EANET likely comes from shortcomings in the temporal profiles of emission inventories and is affected by the distribution of limited measurement sites. A comparison of model outputs from STOCHEM-CRI and WRF-Chem-CRI with satellite observations (Khan et al., 2020) also highlights a poor temporal agreement for NH_3 seasonality. Further model experiments are required to investigate the impacts of different monthly emission and local meteorology on temporal variations of reduced N species.

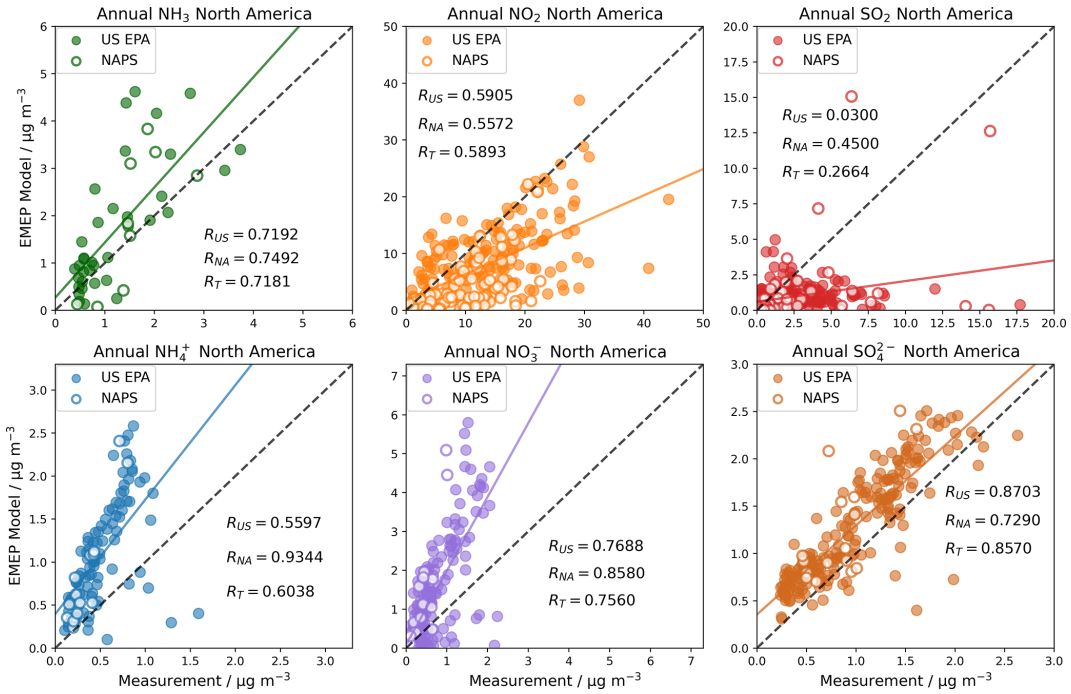

Figure 10. Scatter plots of 2015 annual mean modelled and measured NH_3, NO_2, HNO_3, SO_2, NH_4^+, NO_3^-, and SO_4^{2-} concentrations at North American monitoring network locations. In each plot, the solid line is the least-squares regression line and the dashed black line is the 1 : 1 line. R_{US} is for U.S. EPA network. R_{NA} is for NAPS network. R_T is the overall correlation coefficient between model and all measurements shown.

Table 4. Summary statistics of model comparison with measurements for 2015 in North America (U.S. EPA and NAPS networks). N is the number of paired data of model and observation. R_T is Pearson's coefficient for total measurements in U.S. EPA and NAPS networks. Fac2 is the fraction of data points within a factor of 2. Mean_O and Mean_M are annual average concentrations ($\mu g\,m^{-3}$) of observation and model, respectively. NMB is normalized mean bias, NME is normalized mean error.

Species	N	R_T	Fac2 fraction	Mean_O	Mean_M	NMB	NME
NH_3	45	0.72	0.64	1.28	1.76	0.37	0.57
NO_2	259	0.59	0.55	12.27	7.43	−0.39	0.49
HNO_3	9	0.62	0.78	0.39	0.53	0.36	0.52
SO_2	264	0.27	0.31	2.43	0.96	−0.61	0.75
NH_4^+	106	0.60	0.32	0.50	1.06	1.12	1.25
NO_3^-	212	0.76	0.36	0.58	1.19	1.05	1.32
SO_4^{2-}	216	0.86	0.87	0.97	1.27	0.31	0.36

3.3 Comparisons of modelled precipitation and wet deposition with measurements

The evaluations of model performance for precipitation and wet deposition are based on the four monitoring networks (China, East Asia, Europe, and the United States) that report both precipitation and precipitation concentration measurements for 2015. The total annual wet deposition (WDEP) is calculated as follows:

$$\mathrm{WDEP} = \overline{C} \times \sum P_i,$$

where $\overline{C}$ (also referred to here as Prec Conc) is the precipitation-weighted annual average concentration

$$\overline{C} = \frac{\sum (C_i \times P_i)}{\sum P_i},$$

C_i is the concentration, and P_i is the depth of each individual precipitation event i in the year. Prec Amount, $\sum P_i$, is the total precipitation depth for the year. When C_i (and $\overline{C}$) are expressed in units of milligrams per litre and P_i in millimetres, then WDEP is expressed in units of milligrams per square metre.

Figure 12 shows for each location in each of the five networks the comparisons between modelled and measured

Table 5. Seasonal averages of monthly NH_3 concentrations ($\mu g\,m^{-3}$) for model (Mod) and measurements (Obs) in four monitoring networks: spring, i.e. March, April, May; summer, i.e. June, July, August; autumn, i.e. September, October, November; winter, i.e. December, January, February.

Networks	Spring		Summer		Autumn		Winter	
$\mu g\,m^{-3}$	Obs	Mod	Obs	Mod	Obs	Mod	Obs	Mod
China	10.9	14.6	14.6	14.8	8.72	12.9	6.54	9.09
East Asia	1.99	2.91	1.95	2.64	2.17	2.40	2.02	1.27
UK	1.94	1.71	1.43	2.49	1.36	1.90	1.10	0.61
EMEP/CCC	0.83	1.90	0.82	2.53	0.54	1.77	0.44	0.84

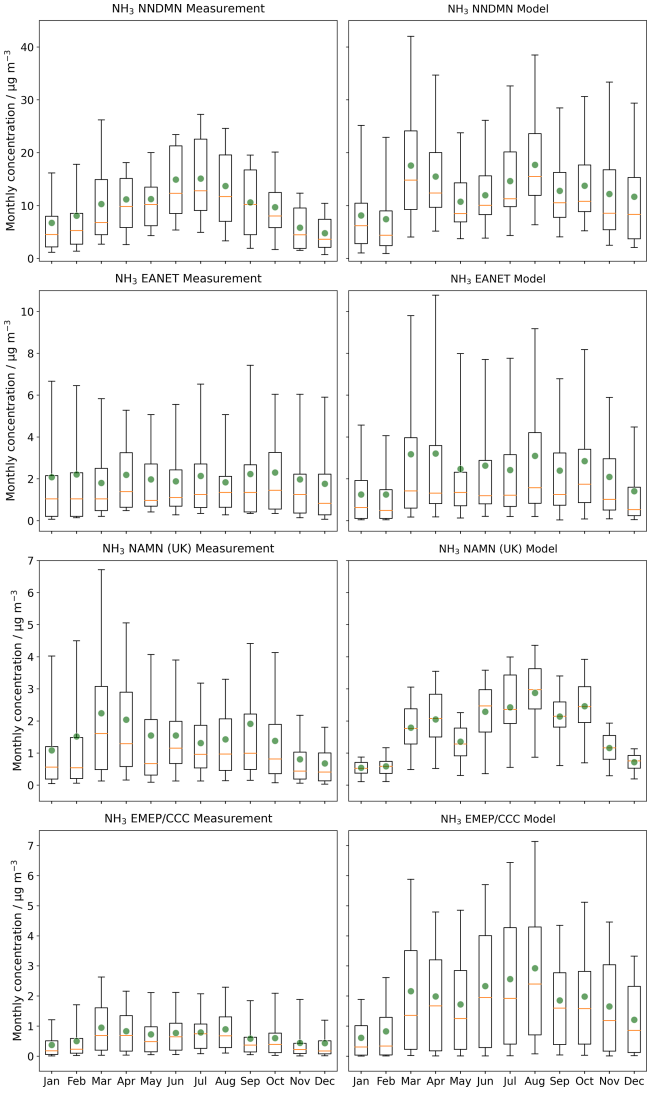

Figure 11. Monthly variations in modelled and measured NH_3 concentrations for locations in four monitoring networks in 2015. The box extends from the lower to upper quartile values of the data, with an orange line at the median and a green point at the mean. The whiskers represent 5 % and 95 % percentiles.

annual precipitation, precipitation-weighted annual average concentration of reduced N (in the form of NH_4^+) and annual total wet deposition of reduced N in 2015. Table 6 summarizes the statistical metrics associated with each comparison. The comparisons of modelled and measured total rainfall show that the model is capable of simulating spatial variations of precipitation over different global regions. The correlation coefficient R between modelled and measured annual precipitation ranges from 0.65 to 0.94 with an average of 0.77. The high Fac2 proportions indicate that the model can simulate the precipitation amount in EANET (82 %), EMEP/CCC (91 %), US NTN (82 %), and Canada CAPMoN (100 %) locations but not so well for NNDMN (43 %). In terms of model–measurement biases, the model underestimates annual precipitation amounts by 13 %–45 %. Given the 1° spatial resolution of the model and the localized nature of precipitation events, such a model underestimation range is expected.

The model performance in precipitation concentrations of reduced N varies between NNDMN and other networks. Whilst comparisons for EANET, EMEP/CCC, US NTN, and Canada CAPMoN show close to 1 : 1 linear relationships with R values all > 0.71, comparison at NNDMN locations shows a relatively poor correlation ($R = 0.45$). This may reflect instrumental and experimental differences between monitoring networks. Considering the limited number of monitoring sites in NNDMN, more measurement data are required to draw a more representative model–measurement comparison in China.

The measured annual wet deposition of reduced N is affected by the quality of the measurement of both collected rainfall and precipitation-weighted average NH_4^+ concentration. Based on measurement locations, NNDMN shows the largest annual reduced N wet deposition for both model ($777\,mg\,N\,m^{-2}$) and measurement ($986\,mg\,N\,m^{-2}$), followed by EANET (model $380\,mg\,N\,m^{-2}$, measurement $499\,mg\,N\,m^{-2}$), EMEP/CCC (model $146\,mg\,N\,m^{-2}$, measurement $226\,mg\,N\,m^{-2}$), Canada CAPMoN (model $144\,mg\,N\,m^{-2}$, measurement $288\,mg\,N\,m^{-2}$), and US NTN (model $135\,mg\,N\,m^{-2}$, measurement $192\,mg\,N\,m^{-2}$). The model simulates lower total reduced N wet depositions by 21 %–50 % across the five networks. This general model un-

derestimation is largely driven by the underestimation of total precipitation, and to less extent the precipitation concentration. Across the five networks, linear correlation between modelled and measured wet deposition of reduced N is best for the Canada CAPMoN network with $R = 0.82$.

The comparison for global wet deposition of total oxidized N (in the form of NO_3^-) exhibits similar results and is presented in the Supplement (Fig. S11 and Table S2). The modelled precipitation-weighted concentrations of NO_3^- has relatively good agreements with measurements in EANET, EMEP/CCC, US NTN, and Canada CAPMoN networks with R ranging from 0.69 to 0.82, while the comparisons in NNDMN show a poorer linear correlation between model and measurement ($R = 0.39$). In terms of biases, the model tends to simulate higher NO_3^- concentrations in precipitations in EANET (NMB = 0.52) and US NTN (NMB = 1.04) networks but underestimate in NNDMN (NMB = −0.37). In general, the greatest model–measurement agreement for oxidized N wet deposition is found in Canada CAPMoN and US NTN, followed by EMEP/CCC and EANET, and to the lowest extent NNDMN, which again suggests systematic differences between monitoring networks rather than issues with the modelling of atmospheric chemistry and meteorology.

On the whole, the modelled reduced and oxidized N show similar linear relationships with measurements in precipitation and wet deposition in all regions, which further supports the utilization of the WRF and EMEP MSC-W modelling system to investigate N_r processes globally.

4 Discussion

The work presented here is motivated by the use of the EMEP MSC-W-WRF model for global-scale analyses of atmospheric nitrogen and SIA chemistry, fluxes, and budget, particularly species that contain reduced N (i.e. gaseous NH_3 and particulate NH_4^+). The model evaluation, conducted both spatially and temporarily, is based on the available data in 2010 and 2015 from nine monitoring networks that span the range of ambient measurements in East Asia, Southeast Asia, Europe, and North America.

Table 7 summarizes the global comparison between model and surface measurements in 2015. The correlation coefficients (R) between modelled and measured concentrations of most species (i.e. NH_3, NO_2, NH_4^+, NO_3^-, and SO_4^{2-}) are all greater than 0.78 except for HNO_3 and SO_2. The correlation coefficient for wet deposition of reduced N and oxidized N is 0.78 and 0.63, respectively. For reduced N species, the evaluation shows that the model overestimates NH_3 and NH_4^+ worldwide with a NMB of 31 % and 37 %, respectively. For oxidized N species, the NMB values for NO_2 and NO_3^- are 23 % and 61 %, and in contrast HNO_3 is underestimated by 34 %. Slightly higher concentrations are also simulated by the model worldwide for both SO_2 and SO_4^{2-} with a NMB of 10 % and 21 %, respectively. For wet deposition, the model outputs smaller values on average for reduced N (NMB = −30 %) compared with measurements, whereas the NMB for oxidized N is only −3 %. Given the intrinsic discrepancies between local site measurement and a global-scale chemistry model grid, these comparisons are good and are comparable with model evaluation statistics determined for models of similar resolution (Hauglustaine et al., 2014; Bellouin et al., 2011; Pringle et al., 2010; Xu and Penner, 2012).

Both model and measurement have uncertainty that constrains the extent to which statistical analyses between modelled and measured data can be utilized to assess a model's performance. A reliable evaluation of a model requires a high quality of measurement as well. For instance, sampling and chemical analysis procedures such as the instrument calibration, the choice of sampling filters/tubes, the storage, extraction, and chemical speciation of air samples all have different uncertainties propagated to the final measured variable. In particular, this study and the above-mentioned global modelling studies all show difficulties in representing surface NO_3^- and NH_4^+ concentrations, which are currently overestimated by around a factor of 2 in Europe and North America. Such positive biases between modelled and measured NO_3^- and NH_4^+ are speculated to be partially associated with negative sampling artefacts in measurements as evaporation of NH_4NO_3 from sampling filters has been reported to cause losses of up to 50 % in summer conditions (Hauglustaine et al., 2014; Vecchi et al., 2009; Yu et al., 2005). Further work is required to better characterize and quantify the uncertainty of individual NO_3^- and NH_4^+ measurements. In general, the relative measurement uncertainty increases markedly as concentration decreases (Thunis et al., 2013; Pernigotti et al., 2013). The EMEP/CCC data report for 2015 estimates a combined sampling and chemical analysis uncertainty range of 15 %–25 % (Hjellbrekke, 2017), while the detailed uncertainty information in other monitoring networks is not publicly available.

Similarly, different input, configurations and computing processors also have influences on the model output, and the quantification of such influence is rather complicated (Kong et al., 2020). The choice of emission input is a good example (Aleksankina et al., 2019). The compilation of an emission inventory is partially based on reported measurement data and partially on expert estimation, which consequently leads to a certain uncertainty in emission magnitudes and temporal profiles (EMEP/EEA, 2019; Hilde Fagerli, 2017; Klimont et al., 2017; Wiedinmyer et al., 2011; Zheng et al., 2012). The completeness and consistency of submitted emission data differs significantly across countries as well. As discussed in Sect. 3.1, the two global emission inventories used in this work, HTAP and $ECLIPSE_E$, have shown large localized discrepancies in NH_3, NO_2, and SO_2 emissions in certain world regions, which is presumably ascribable to the inclusion or exclusion of a particular local point source in the compilation process. The influence of these discrepancies

Table 6. Summary statistics of model comparison with measurements for annual precipitation (Prec Amount, mm), precipitation-weighted mean concentration of NH_4^+ (Prec Conc, mg N L^{-1}), and wet deposition of reduced N (WDEP, mg N m^{-2}) in 2015. *N* is the number of measuring sites. *R* is Pearson's coefficient. Fac2 is the fraction of data points that are within a factor of 2. Mean_O and Mean_M of Prec Conc are annual averages of observation and model, respectively. Mean_O and Mean_M of Prec Amount and WDEP are annual totals. NMB is normalized mean bias, and NME is normalized mean error.

Networks	Variables	*N*	*R*	Fac2 fraction	Mean_O	Mean_M	NMB	NME
China	Prec Amount	21	0.73	0.43	913	502	−0.45	0.49
	Prec Conc	21	0.45	0.71	2.00	2.18	0.09	0.45
	WDEP	21	0.59	0.62	986	777	−0.21	0.42
East Asia	Prec Amount	50	0.65	0.82	1585	1270	−0.20	0.39
	Prec Conc	44	0.71	0.66	0.44	0.42	−0.04	0.62
	WDEP	40	0.68	0.62	499	380	−0.24	0.50
Europe	Prec Amount	101	0.78	0.91	863	749	−0.13	0.31
	Prec Conc	89	0.77	0.85	0.32	0.26	−0.19	0.28
	WDEP	89	0.61	0.75	226	146	−0.35	0.41
United States	Prec Amount	206	0.73	0.82	1030	690	−0.33	0.39
	Prec Conc	207	0.76	0.90	0.22	0.22	0.03	0.30
	WDEP	206	0.75	0.81	192	135	−0.30	0.36
Canada	Prec Amount	28	0.94	1.00	941	632	−0.33	0.33
	Prec Conc	28	0.85	0.86	0.32	0.25	−0.22	0.29
	WDEP	28	0.82	0.57	288	144	−0.50	0.50

Table 7. Summary statistics of global model evaluation of atmospheric concentrations (µg m^{-3}), annual precipitation (Prec Amount, mm), precipitation-weighted mean concentration of NH_4^+ and NO_3^- (Prec Conc, mg N L^{-1}), and wet deposition (mg N m^{-2}) of reduced N (RDN) and oxidized N (OXN) in 2015. *N* is the number of measuring sites. *R* is Pearson's correlation coefficient. Fac2 is the fraction of data points that are within a factor of 2. Mean_O and Mean_M of Prec Conc are annual averages of observation and model, respectively. Mean_O and Mean_M of Prec Amount and WDEP are annual totals. NMB is normalized mean bias, NME is normalized mean error.

Globe	Variables	*N*	*R*	Fac2 fraction	Mean_O	Mean_M	NMB	NME
Atmospheric concentration	NH_3	173	0.85	0.57	2.55	3.35	0.31	0.63
	NO_2	372	0.78	0.62	7.43	9.11	0.23	0.56
	HNO_3	109	0.54	0.50	1.44	0.95	−0.34	0.68
	SO_2	390	0.61	0.45	1.05	1.16	0.10	0.82
	NH_4^+	230	0.83	0.43	1.31	1.80	0.37	0.69
	NO_3^-	334	0.83	0.40	1.41	2.28	0.61	0.88
	SO_4^{2-}	320	0.83	0.81	1.17	1.42	0.21	0.38
Wet deposition (RDN)	Prec amount	403	0.74	0.83	1044	763	−0.27	0.37
	Prec conc	386	0.80	0.85	0.37	0.36	−0.03	0.38
	WDEP	381	0.78	0.75	278	194	−0.30	0.42
Wet deposition (OXN)	Prec conc	392	0.79	0.61	0.30	0.35	0.15	0.56
	WDEP	389	0.63	0.83	218	212	−0.03	0.45

on model-simulated surface concentration differs in terms of primary or secondary component and varies from one region to another, although such greatly localized influences are diminished during the spatial averaging processes. It is therefore important to acknowledge that the performance of any model is subject to the quality of model input data, which includes not only emissions but also meteorology and other aspects of model parameters. Moreover, no one can guarantee error-free models; in the same way that observations are likely to be not error free. Often in the atmospheric modelling community these potential model errors are not discussed or acknowledged.

Aside from intrinsic uncertainties in model and/or measurement values, the model and measurement may also not agree concerning the averaging time periods and the diameters of the sampled particles. A certain number of measure-

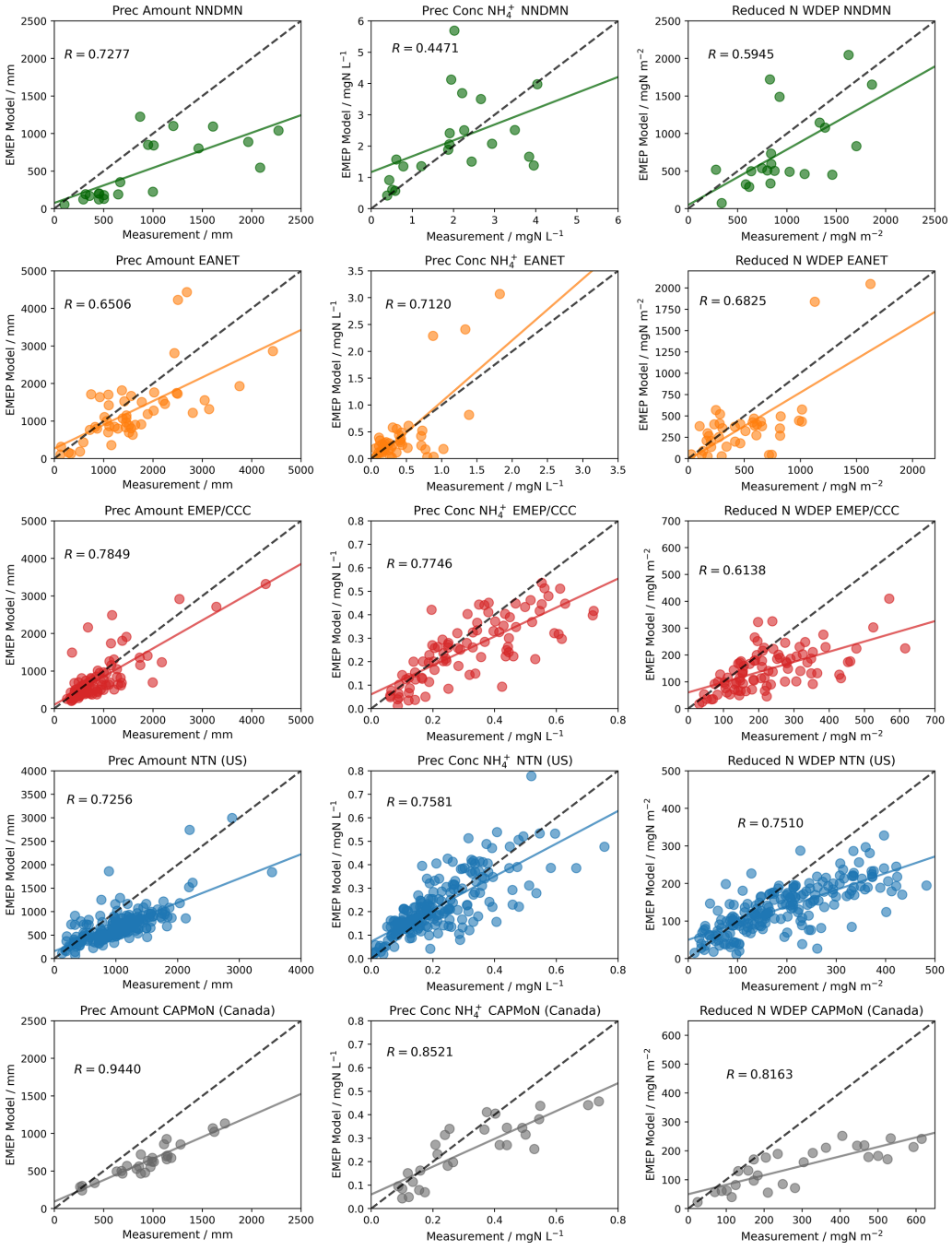

Figure 12. Scatter plots of model–measurement comparisons of 2015 annual wet deposition variables for reduced N (in the form of NH_4^+) for five measurement networks: NNDMN, EANET, EMEP/CCC, US NTN, and Canada CAPMoN. The left column shows annual precipitation. The middle column shows precipitation-weighted annual average NH_4^+ concentration in precipitation. The right column shows annual total wet deposition of NH_4^+. In each plot, the coloured line is the least-squares regression, and the dashed black line is the 1 : 1 line.

ments may be missing from a time series due to unpredictable instrument failure and/or because the measurement averaging period does not exactly match the model averaging time period. It is clear that the sampling time and size distributions of measurements vary from one monitoring network to another and from species to species. For example, in Canada, NH_4^+ concentrations within $PM_{2.5}$ are measured, while the particle size cut-off for the DELTA system used in the UK and China is around 4.5 µm (Tang et al., 2018a, b; Xu et al., 2019). The modelled NH_4^+, SO_4^{2-}, and fine NO_3^- are all in $PM_{2.5}$. Another example is that in the US and Canada gaseous species like NO_2 and SO_2 are monitored continually

throughout the year and thus the corresponding annual average concentrations are calculated in the same way as the model, whilst the aerosol components such as NO_3^- and NH_4^+ are measured once per 6 d (or once per week). In addition, different networks, and even different sites in the same network, may measure at different frequencies and at different times, which presents inherent practical difficulties in comparing model simulations with ambient measurements. Further moves towards global standardized approaches for measurements across different networks is encouraged.

Even if both model and measurement were perfect representations, there still would not be complete agreement because a measurement is for a single point in space, whereas even for models with high spatial resolution, model output is a volume average. For a global model simulation with grid resolution of $1^\circ \times 1^\circ$, the monitoring site simply samples the air in one part of that grid volume and at a specific height above the ground, which may often not reflect the average concentration for the grid. Indeed, there are particular monitoring sites where measurements are exceedingly affected by local sources. The UK NAMN is a good example, in which quite a few sites are purposely set near agricultural sources and therefore yield higher NH_3 concentrations than model grid-average predictions. The U.S. EPA also has many monitors set up next to roads with heavy traffic and hence observed much higher SO_2 levels. The representativeness of an urban (or rural) site for the air in the corresponding model grid will therefore depend on the relative size of that specific urban (or rural) area within that model grid.

The intention here is to provide an overview of how the EMEP-WRF model–measurement agreements vary among different monitoring networks and among different chemical species for evaluation of a chemistry transport model in a global context. In general, the model shows better linear correlations with surface concentration measurements in East Asia ($\overline{R} = 0.73$ over seven species), Europe ($\overline{R} = 0.67$ over seven species), and North America ($\overline{R} = 0.63$ over seven species) than in China ($\overline{R} = 0.35$ over five species). More specifically, comparisons in China show the model performs better in computing concentrations of primary pollutants (i.e. NH_3 and NO_2) than secondary species (i.e. NH_4^+ and NO_3^-), while the model evaluation statistics in East Asia, Europe, and North America show almost equally good results over all species. This implies potential discrepancies in the measurements or emissions in China rather than general issues with meteorological and atmospheric chemistry modelling. The values of statistical metrics in this work are as good as other global model evaluation studies. A global model aerosol simulation study (Hauglustaine et al., 2014) reported that the R of global model results (LMDz-INCA global chemistry–aerosol–climate model, 1.9° latitude × 3.75° longitude resolution) versus measurements in 2006 for surface concentrations of SO_4^{2-}, NH_4^+ and NO_3^- ranged from 0.43 to 0.58 in Europe and from 0.54 to 0.77 in North America, which is similar to our results presented here. The AeroCom phase III global nitrate experiment, which includes nine models, reported slightly lower R ranges than here for annual NO_3^- in 2008: 0.081–0.735 in North America, 0.393–0.585 in Europe, and 0.226–0.429 in Southeast Asia (Bian et al., 2017); and the agreements between model and observation for gas tracers in that study were even lower than here.

This work has utilized the EMEP MSC-W v4.34 coupled with WRF v3.9.1.1 model. As discussed above, model–measurement comparison statistics will vary in different global models to different extent. However, the broad discussions associated with fundamental differences between localized measurement and grid-volume-averaged model output, inconsistent temporal coverage, relatively high uncertainties of emissions, and intrinsic limitations of measurement are generalizable, as atmospheric chemistry and transport models and other climate models are constructed similarly. Allowance for these inherent model–measurement discrepancies and uncertainties yield significantly less stringent requirements on acceptable model evaluation statistics than might initially be expected. Urban dispersion models (Denby et al., 2020; Hood et al., 2018) with higher resolutions have stronger capabilities of representing point sources and concentration gradients but are constrained even more by the accuracy of localized emission inventories and boundary conditions in the meantime, and therefore are only configured at an individual urban area. Global-scale model simulation as presented here, in spite of acknowledged limitations on coarser spatial resolution, has the advantage of generating self-consistent chemistry fields and competence for investigating contemporary and potential future global reactive nitrogen and SIA atmospheric chemistry and their regional variations.

5 Conclusions

This model versus measurement study is motivated by the first application of a global version of the EMEP MSC-W model with WRF meteorology ($1^\circ \times 1^\circ$ horizontal resolution) to study global reactive N and S chemistry and deposition. A comprehensive spatial and temporal comparison of model output against 10 monitoring networks from four world regions (East Asia, Southeast Asia, Europe, and North America) has been undertaken, with a focus on the atmospheric concentrations and wet deposition of major inorganic pollutants and on reduced nitrogen components in particular. Simulations were performed with EMEP MSC-W model version 4.34 with WRF 3.9.1.1 meteorology, using both $ECLIPSE_E$ (2010 and 2015) and HTAP (2010 only) emission inventories; $ECLIPSE_E$ refers to ECLIPSE annual emissions with EDGAR monthly profiles.

In general, simulations of annual surface concentrations of a primary pollutant such as NH_3 are somewhat sensitive to the choice of HTAP or $ECLIPSE_E$ emission inven-

tories in places where regional differences in primary emissions between the two emission inventories are apparent, e.g. China. By comparison, the impact of difference between the emissions inventories on concentrations of secondary species such as NH_4^+ is much smaller. The difference in 2010 global area-weighted annual average NH_3 concentration is $0.05\,\mu g\,m^{-3}$ (HTAP: $0.26\,\mu g\,m^{-3}$; $ECLIPSE_E$: $0.31\,\mu g\,m^{-3}$), which is 18 % of the absolute concentration, whilst the NH_4^+ concentration difference is only $0.02\,\mu g\,m^{-3}$ or only 3.5 % of the global average concentrations (HTAP: $0.316\,\mu g\,m^{-3}$; $ECLIPSE_E$: $0.305\,\mu g\,m^{-3}$). In terms of temporal profiles, the monthly average emissions vary similarly throughout the year in the four world regions after the monthly profiles derived from EDGAR are applied to the ECLIPSE annual total emissions.

Comparisons of 2010 and 2015 annual average concentrations between model and measurement demonstrate that the model captures the overall spatial and temporal variations of major inorganic pollutants well despite spanning large concentration ranges in different world regions. The discussion of model evaluation statistics mainly focuses on 2015 as the results for 2010 are similar.

In general, capturing correlation is more important than bias given the intrinsic discrepancies and uncertainties between the modelled and measured variables. In this work the model shows better linear correlations with measurement networks in Southeast Asia (Mean R for seven species: $\overline{R_7} = 0.73$), Europe ($\overline{R_7} = 0.67$), and North America ($\overline{R_7} = 0.63$) than in China ($\overline{R_5} = 0.35$ over five species), which implies potential discrepancies with some measurements and emissions rather than issues with modelling meteorological and atmospheric chemistry processes. Model–measurement bias varies from one species to another in different networks. NH_4^+ and NO_3^- are the species overestimated the most by the model in Europe and North America but not so much in East Asian and Southeast Asian networks, reflecting that the model production of the two species might be too fast and/or the chemical and physical losses might be too slow in the two regions. The model performs the best in simulating SO_4^{2-} concentrations in North America regarding overall statistics among various species in all networks.

Both model and measurement exhibit higher NH_3 concentrations in spring and summer, and lower concentrations in winter. The greatest agreement of temporal profile for model and measurement is found in Europe. The fluctuation of monthly average NH_3 concentrations in Southeast Asia throughout the year 2015 is fairly small for both model and measurement and the temporal trend is therefore less clear. Small differences appear regarding the specific peak concentration months in China and UK. Measurements in China show highest monthly concentration in July, while the model simulates two peaks in August and March. The highest NH_3 concentrations in the UK network are in spring, whereas the modelled concentrations peak in summer. Such disagreements again reflect the likelihood that the major driver of model discrepancies is the inaccuracy of temporal profiles of emissions rather than the simulation of atmospheric chemistries and physics.

The evaluation of wet deposition shows that the model is capable of simulating spatial variation of annual precipitation correctly in all four world regions (0.65–0.94 R range) despite a 13 %–45 % underestimation. Given that the spatial and temporal averaging smooths out highly localized effects of precipitation event, such model–measurement discrepancy is reasonable. In respect of the weighted precipitation concentrations, high linear correlations between measured and modelled NH_4^+ and NO_3^- concentrations are observed in Southeast Asia, Europe, and North America but not China, which may again suggest a systematic difference among measurements rather than models. In general, the model shows the greatest consistency of annual total wet deposition with measurements in North America (R: 0.75–0.82 and 0.81–0.81 for reduced and oxidized N, respectively), followed by Southeast Asia (R: 0.68 and 0.51), Europe (R: 0.61 and 0.64), and China (R: 0.59 and 0.13).

Despite discussed limitations in model-measurement comparisons, the detailed evaluations presented here support the utilization of this global implementation of the EMEP MSC-W-WRF coupled model for analyses of surface concentrations and wet depositions of major reactive N and S species in different world regions. Modelling of atmospheric chemistry and transport on the global scale has the advantage of providing consistent data with comprehensive spatial and temporal coverage, of filling in the research gap in global model evaluation, and of facilitating investigation of global reactive N and SIA deposition budgets and chemistry- and policy-oriented model experiments for potential future scenarios.

Code and data availability. As described and referenced in Sect. 2 of this paper, this study used two open-source global models: the European Monitoring and Evaluation Programme Meteorological Synthesizing Centre – West atmospheric chemistry transport model (EMEP MSC-W, 2020, version 4.34; source code available at https://doi.org/10.5281/zenodo.3647990) and the Weather Research and Forecast meteorological model (WRF, version 3.9.1.1, http://www.wrf-model.org, last access: 20 May 2021, Skamarock et al., 2008, https://doi.org/10.5065/D68S4MVH). The two global emission inventories applied are described in Sect. 2.1. All measurement datasets used in this work are publicly available, and their individual websites are listed in Sect. 2.2. The model and measurement output presented in figures and tables in this paper and the corresponding Python scripts are available at https://doi.org/10.5281/zenodo.5037080 (Ge, 2021).

Supplement. The supplement related to this article is available online at: https://doi.org/10.5194/gmd-14-7021-2021-supplement.

Author contributions. MRH, DSS, and MV conceptualized and supervised the study. MV and PW contributed to the model development and set-up and provided modelling support. MV provided computing resources. YG contributed to study design, undertook all model simulations, compiled measurement datasets, performed formal data analyses, created visualization of the results, and curated the data, with discussion and refinement by all authors. The original draft of the paper was written by YG with editing by MRH. All authors provided review comments and approved the final version.

Competing interests. The contact author has declared that neither they nor their co-authors have any competing interests.

Disclaimer. Publisher's note: Copernicus Publications remains neutral with regard to jurisdictional claims in published maps and institutional affiliations.

Acknowledgements. Yao Ge gratefully acknowledges studentship funding from the University of Edinburgh and its School of Chemistry. This work was in part supported by the UK Natural Environment Research Council (NERC), including grant nos. NE/R016429/1 and NE/R000131/1, as part of the UK-SCAPE and SUNRISE programmes delivering UK National Capability, and the European Modelling and Evaluation Programme under the United Nations Economic Commission for Europe Convention on Long-range Transboundary Air Pollution.

Financial support. This research has been supported by the Natural Environment Research Council (grant nos. NE/R016429/1 and NE/R000131/1) and the University of Edinburgh (PhD studentship).

Review statement. This paper was edited by Fiona O'Connor and reviewed by two anonymous referees.

References

Adams, P. J., Seinfeld, J. H., and Koch, D. M.: Global concentrations of tropospheric sulfate, nitrate, and ammonium aerosol simulated in a general circulation model, J. Geophys. Res.-Atmos., 104, 13791–13823, https://doi.org/10.1029/1999JD900083, 1999.

Aleksankina, K., Reis, S., Vieno, M., and Heal, M. R.: Advanced methods for uncertainty assessment and global sensitivity analysis of an Eulerian atmospheric chemistry transport model, Atmos. Chem. Phys., 19, 2881–2898, https://doi.org/10.5194/acp-19-2881-2019, 2019.

Bellouin, N., Rae, J., Jones, A., Johnson, C., Haywood, J., and Boucher, O.: Aerosol forcing in the Climate Model Intercomparison Project (CMIP5) simulations by HadGEM2-ES and the role of ammonium nitrate, J. Geophys. Res., 116, D20206, https://doi.org/10.1029/2011JD016074, 2011.

Bergström, R., Hallquist, M., Simpson, D., Wildt, J., and Mentel, T. F.: Biotic stress: a significant contributor to organic aerosol in Europe?, Atmos. Chem. Phys., 14, 13643–13660, https://doi.org/10.5194/acp-14-13643-2014, 2014.

Bergström, R., Jenkin, M., Hayman, G., and Simpson, D.: Update and comparison of atmospheric chemistry mechanisms for the EMEP MSC-W model system – EmChem19a, EmChem19X, CRIv2R5Em, CB6r2Em, and MCMv3.3Em, in preparation, 2021.

Bian, H., Chin, M., Hauglustaine, D. A., Schulz, M., Myhre, G., Bauer, S. E., Lund, M. T., Karydis, V. A., Kucsera, T. L., Pan, X., Pozzer, A., Skeie, R. B., Steenrod, S. D., Sudo, K., Tsigaridis, K., Tsimpidi, A. P., and Tsyro, S. G.: Investigation of global particulate nitrate from the AeroCom phase III experiment, Atmos. Chem. Phys., 17, 12911–12940, https://doi.org/10.5194/acp-17-12911-2017, 2017.

Burnett, R., Chen, H., Szyszkowicz, M., Fann, N., Hubbell, B., Pope, C. A., Apte, J. S., Brauer, M., Cohen, A., Weichenthal, S., Coggins, J., Di, Q., Brunekreef, B., Frostad, J., Lim, S. S., Kan, H., Walker, K. D., Thurston, G. D., Hayes, R. B., Lim, C. C., Turner, M. C., Jerrett, M., Krewski, D., Gapstur, S. M., Diver, W. R., Ostro, B., Goldberg, D., Crouse, D. L., Martin, R. V., Peters, P., Pinault, L., Tjepkema, M., van Donkelaar, A., Villeneuve, P. J., Miller, A. B., Yin, P., Zhou, M., Wang, L., Janssen, N. A. H., Marra, M., Atkinson, R. W., Tsang, H., Quoc Thach, T., Cannon, J. B., Allen, R. T., Hart, J. E., Laden, F., Cesaroni, G., Forastiere, F., Weinmayr, G., Jaensch, A., Nagel, G., Concin, H., and Spadaro, J. V.: Global estimates of mortality associated with long-term exposure to outdoor fine particulate matter, P. Natl. Acad. Sci. USA, 115, 9592, https://doi.org/10.1073/pnas.1803222115, 2018.

Byun, D. and Schere, K. L.: Review of the Governing Equations, Computational Algorithms, and Other Components of the Models-3 Community Multiscale Air Quality (CMAQ) Modeling System, Appl. Mech. Rev., 59, 51–77, 2006.

Carozzi, M., Loubet, B., Acutis, M., Rana, G., and Ferrara, R. M.: Inverse dispersion modelling highlights the efficiency of slurry injection to reduce ammonia losses by agriculture in the Po Valley (Italy), Agr. Forest Meteorol., 171–172, 306–318, https://doi.org/10.1016/j.agrformet.2012.12.012, 2013.

Chapman, E. G., Gustafson Jr., W. I., Easter, R. C., Barnard, J. C., Ghan, S. J., Pekour, M. S., and Fast, J. D.: Coupling aerosol-cloud-radiative processes in the WRF-Chem model: Investigating the radiative impact of elevated point sources, Atmos. Chem. Phys., 9, 945–964, https://doi.org/10.5194/acp-9-945-2009, 2009.

Cheng, Y., Duan, F.-k., He, K.-b., Du, Z.-y., Zheng, M., and Ma, Y.-l.: Sampling artifacts of organic and inorganic aerosol: Implications for the speciation measurement of particulate matter, Atmos. Environ., 55, 229–233, https://doi.org/10.1016/j.atmosenv.2012.03.032, 2012.

Ciarelli, G., Theobald, M. R., Vivanco, M. G., Beekmann, M., Aas, W., Andersson, C., Bergström, R., Manders-Groot, A., Couvidat, F., Mircea, M., Tsyro, S., Fagerli, H., Mar, K., Raffort, V., Roustan, Y., Pay, M.-T., Schaap, M., Kranenburg, R., Adani, M., Briganti, G., Cappelletti, A., D'Isidoro, M., Cuvelier, C., Cholakian, A., Bessagnet, B., Wind, P., and Colette, A.: Trends of inorganic and organic aerosols and precursor gases in Europe: insights from the EURODELTA multi-model experiment

over the 1990–2010 period, Geosci. Model Dev., 12, 4923–4954, https://doi.org/10.5194/gmd-12-4923-2019, 2019.

Crippa, M., Solazzo, E., Huang, G., Guizzardi, D., Koffi, E., Muntean, M., Schieberle, C., Friedrich, R., and Janssens-Maenhout, G.: High resolution temporal profiles in the Emissions Database for Global Atmospheric Research, Sci. Data, 7, 121, https://doi.org/10.1038/s41597-020-0462-2, 2020.

Denby, B. R., Gauss, M., Wind, P., Mu, Q., Grøtting Wærsted, E., Fagerli, H., Valdebenito, A., and Klein, H.: Description of the uEMEP_v5 downscaling approach for the EMEP MSC-W chemistry transport model, Geosci. Model Dev., 13, 6303–6323, https://doi.org/10.5194/gmd-13-6303-2020, 2020.

EMEP/EEA: EMEP/EEA air pollutant emission inventory guidebook, European Environment Agency, Luxembourg, 15 pp., 2019.

EMEP MSC-W: metno/emep-ctm: OpenSource rv4.34 (202001), rv4_34, Zenodo [code], https://doi.org/10.5281/zenodo.3647990, 2020.

Erisman, J. W., Domburg, N., de Vries, W., Kros, H., de Haan, B., and Sanders, K.: The Dutch N-cascade in the European perspective, Sci. China Ser. C, 48, 827–842, 2005.

Fagerli, H., Tsyro, S., Denby, B. R., Nyíri, Á., Gauss, M., Simpson, D., Wind, P., Benedictow, A., Jonson, J. E., Klein, H., Schulz, M., Griesfeller, J., Aas, W., Hjellbrekke, A.-G., Solberg, S., Platt, S. M., Fiebig, M., Yttri, K. E., Rud, R. O., Tørseth, K., Mareckova, K., Pinterits, M., Tista, M., Ullrich, B., and Wankmüller, R.: EMEP Status Report 1/2017: Transboundary particulate matter, photo-oxidants, acidifying and eutrophying components (Joint MSC-W & CCC & CEIP Report), Meteorological Synthesizing Centre-West of EMEP(MSC-W of EMEP), European Monitoring and Evaluation Programme (EMEP), 41, 2017.

Fagerli, H., Tsyro, S., Jonson, J. E., Nyíri, Á., Gauss, M., Simpson, D., Wind, P., Benetictow, A., Klein, H., Mortier, A., Aas, W., Hjellbrekke, A.-G., Solberg, S., Platt, S. M., Yttri, K. E., Tørseth, K., Gaisbauer, S., Mareckova, K., Matthews, B., Schindlbacher, S., Sosa, C., Tista, M., Ullrich, B., Wankmüller, R., Scheuschner, T., Bergström, R., Johanson, L., Jalkanen, J.-P., Metzger, S., van der Gon, H. A. C. D., Kuenen, J. J. P., Visschedijk, A. J. H., Barregård, L., Molnár, P., and Stockfelt, L.: Updates to the EMEP MSC-W model, 2018–2019, in: Transboundary particulate matter, photo-oxidants, acidifying and eutrophying components, Meteorologisk Institutt – Norwegian Meteorological Institute, Oslo, Norway, 15046109 (ISSN), 44, 2019.

Ge, Y.: Dataset for evaluation of global EMEP MSC-W (rv4.34)-WRF (v3.9.1.1) model surface concentrations and wet deposition of reactive N and S with measurements, Zenodo [data set], https://doi.org/10.5281/zenodo.5037080, 2021.

Gusev, A., MacLeod, M., and Bartlett, P.: Intercontinental transport of persistent organic pollutants: a review of key findings and recommendations of the task force on hemispheric transport of air pollutants and directions for future research, Atmos. Pollut. Res., 3, 463–465, https://doi.org/10.5094/APR.2012.053, 2012.

Hauglustaine, D. A., Balkanski, Y., and Schulz, M.: A global model simulation of present and future nitrate aerosols and their direct radiative forcing of climate, Atmos. Chem. Phys., 14, 11031–11063, https://doi.org/10.5194/acp-14-11031-2014, 2014.

Hjellbrekke, A.-G.: Data Report 2015 Particulate matter, carbonaceous and inorganic compounds, EMEP Co-operative Programme for Monitoring and Evaluation of the Long-range Transmission of Air Pollutants in Europe, Chemical Co-ordinating Centre of EMEP (CCC), EMEP/CCC Reports, 143 pp., 2017.

Hood, C., MacKenzie, I., Stocker, J., Johnson, K., Carruthers, D., Vieno, M., and Doherty, R.: Air quality simulations for London using a coupled regional-to-local modelling system, Atmos. Chem. Phys., 18, 11221–11245, https://doi.org/10.5194/acp-18-11221-2018, 2018.

Janssens-Maenhout, G., Crippa, M., Guizzardi, D., Dentener, F., Muntean, M., Pouliot, G., Keating, T., Zhang, Q., Kurokawa, J., Wankmüller, R., Denier van der Gon, H., Kuenen, J. J. P., Klimont, Z., Frost, G., Darras, S., Koffi, B., and Li, M.: HTAP_v2.2: a mosaic of regional and global emission grid maps for 2008 and 2010 to study hemispheric transport of air pollution, Atmos. Chem. Phys., 15, 11411–11432, https://doi.org/10.5194/acp-15-11411-2015, 2015.

Jonson, J. E., Borken-Kleefeld, J., Simpson, D., Nyíri, A., Posch, M., and Heyes, C.: Impact of excess NO x emissions from diesel cars on air quality, public health and eutrophication in Europe, Environ. Res. Lett., 12, 094017, https://doi.org/10.1088/1748-9326/aa8850, 2017.

Karl, M., Jonson, J. E., Uppstu, A., Aulinger, A., Prank, M., Sofiev, M., Jalkanen, J.-P., Johansson, L., Quante, M., and Matthias, V.: Effects of ship emissions on air quality in the Baltic Sea region simulated with three different chemistry transport models, Atmos. Chem. Phys., 19, 7019–7053, https://doi.org/10.5194/acp-19-7019-2019, 2019.

Khan, M. A. H., Lowe, D., Derwent, R. G., Foulds, A., Chhantyal-Pun, R., McFiggans, G., Orr-Ewing, A. J., Percival, C. J., and Shallcross, D. E.: Global and regional model simulations of atmospheric ammonia, Atmos. Res., 234, 104702, https://doi.org/10.1016/j.atmosres.2019.104702, 2020.

Klimont, Z., Kupiainen, K., Heyes, C., Purohit, P., Cofala, J., Rafaj, P., Borken-Kleefeld, J., and Schöpp, W.: Global anthropogenic emissions of particulate matter including black carbon, Atmos. Chem. Phys., 17, 8681–8723, https://doi.org/10.5194/acp-17-8681-2017, 2017.

Kong, L., Tang, X., Zhu, J., Wang, Z., Fu, J. S., Wang, X., Itahashi, S., Yamaji, K., Nagashima, T., Lee, H.-J., Kim, C.-H., Lin, C.-Y., Chen, L., Zhang, M., Tao, Z., Li, J., Kajino, M., Liao, H., Wang, Z., Sudo, K., Wang, Y., Pan, Y., Tang, G., Li, M., Wu, Q., Ge, B., and Carmichael, G. R.: Evaluation and uncertainty investigation of the NO_2, CO and NH_3 modeling over China under the framework of MICS-Asia III, Atmos. Chem. Phys., 20, 181–202, https://doi.org/10.5194/acp-20-181-2020, 2020.

Laskin, A., Laskin, J., and Nizkorodov, S. A.: Chemistry of atmospheric brown carbon, Chem. Rev., 115, 4335–4382, 2015.

Li, C., Martin, R. V., van Donkelaar, A., Boys, B. L., Hammer, M. S., Xu, J.-W., Marais, E. A., Reff, A., Strum, M., Ridley, D. A., Crippa, M., Brauer, M., and Zhang, Q.: Trends in Chemical Composition of Global and Regional Population-Weighted Fine Particulate Matter Estimated for 25 Years, Environ. Sci. Technol., 51, 11185–11195, https://doi.org/10.1021/acs.est.7b02530, 2017.

Lin, Y. and Colle, B. A.: A New Bulk Microphysical Scheme That Includes Riming Intensity and Temperature-Dependent Ice Characteristics, Mon. Weather Rev., 139, 1013–1035, https://doi.org/10.1175/2010MWR3293.1, 2011.

Liu, L., Zhang, X., Wong, A. Y. H., Xu, W., Liu, X., Li, Y., Mi, H., Lu, X., Zhao, L., Wang, Z., Wu, X., and Wei, J.: Es-

timating global surface ammonia concentrations inferred from satellite retrievals, Atmos. Chem. Phys., 19, 12051–12066, https://doi.org/10.5194/acp-19-12051-2019, 2019.

McFiggans, G., Mentel, T. F., Wildt, J., Pullinen, I., Kang, S., Kleist, E., Schmitt, S., Springer, M., Tillmann, R., Wu, C., Zhao, D., Hallquist, M., Faxon, C., Le Breton, M., Hallquist, Å. M., Simpson, D., Bergström, R., Jenkin, M. E., Ehn, M., Thornton, J. A., Alfarra, M. R., Bannan, T. J., Percival, C. J., Priestley, M., Topping, D., and Kiendler-Scharr, A.: Secondary organic aerosol reduced by mixture of atmospheric vapours, Nature, 565, 587–593, https://doi.org/10.1038/s41586-018-0871-y, 2019.

Mills, G., Sharps, K., Simpson, D., Pleijel, H., Broberg, M., Uddling, J., Jaramillo, F., Davies, W. J., Dentener, F., Van den Berg, M., Agrawal, M., Agrawal, S. B., Ainsworth, E. A., Büker, P., Emberson, L., Feng, Z., Harmens, H., Hayes, F., Kobayashi, K., Paoletti, E., and Van Dingenen, R.: Ozone pollution will compromise efforts to increase global wheat production, Glob. Change Biol., 24, 3560–3574, https://doi.org/10.1111/gcb.14157, 2018.

Pernigotti, D., Gerboles, M., Belis, C. A., and Thunis, P.: Model quality objectives based on measurement uncertainty. Part II: NO_2 and PM_{10}, Atmos. Environ., 79, 869–878, https://doi.org/10.1016/j.atmosenv.2013.07.045, 2013.

Pommier, M., Fagerli, H., Schulz, M., Valdebenito, A., Kranenburg, R., and Schaap, M.: Prediction of source contributions to urban background PM_{10} concentrations in European cities: a case study for an episode in December 2016 using EMEP/MSC-W rv4.15 and LOTOS-EUROS v2.0 – Part 1: The country contributions, Geosci. Model Dev., 13, 1787–1807, https://doi.org/10.5194/gmd-13-1787-2020, 2020.

Pringle, K. J., Tost, H., Message, S., Steil, B., Giannadaki, D., Nenes, A., Fountoukis, C., Stier, P., Vignati, E., and Lelieveld, J.: Description and evaluation of GMXe: a new aerosol submodel for global simulations (v1), Geosci. Model Dev., 3, 391–412, https://doi.org/10.5194/gmd-3-391-2010, 2010.

Pye, H. O. T., Liao, H., Wu, S., Mickley, L. J., Jacob, D. J., Henze, D. K., and Seinfeld, J. H.: Effect of changes in climate and emissions on future sulfate-nitrate-ammonium aerosol levels in the United States, J. Geophys. Res.-Atmos., 114, D01205, https://doi.org/10.1029/2008JD010701, 2009.

Saha, S., Moorthi, S., Pan, H.-L., Wu, X., Wang, J., Nadiga, S., Tripp, P., Kistler, R., Woollen, J., Behringer, D., Liu, H., Stokes, D., Grumbine, R., Gayno, G., Wang, J., Hou, Y.-T., Chuang, H.-y., Juang, H.-M. H., Sela, J., Iredell, M., Treadon, R., Kleist, D., Van Delst, P., Keyser, D., Derber, J., Ek, M., Meng, J., Wei, H., Yang, R., Lord, S., van den Dool, H., Kumar, A., Wang, W., Long, C., Chelliah, M., Xue, Y., Huang, B., Schemm, J.-K., Ebisuzaki, W., Lin, R., Xie, P., Chen, M., Zhou, S., Higgins, W., Zou, C.-Z., Liu, Q., Chen, Y., Han, Y., Cucurull, L., Reynolds, R. W., Rutledge, G., and Goldberg, M.: The NCEP Climate Forecast System Reanalysis, B. Am. Meteorol. Soc., 91, 1015–1058, https://doi.org/10.1175/2010BAMS3001.1, 2010.

Skamarock, W. C., Klemp, J. B., Dudhia, J., Gill, D. O., Barker, D., Duda, M. G., Huang, X.-y., Wang, W., and Powers, J. G.: A Description of the Advanced Research WRF Version 3 (No. NCAR/TN-475+STR), University Corporation for Atmospheric Research, https://doi.org/10.5065/D68S4MVH, 2008 (data available at: http://www.wrf-model.org, last access: 20 May 2021).

Shaddick, G., Thomas, M. L., Mudu, P., Ruggeri, G., and Gumy, S.: Half the world's population are exposed to increasing air pollution, npj Climate and Atmospheric Science, 3, 23, https://doi.org/10.1038/s41612-020-0124-2, 2020.

Sickles, I. J. E., Hodson, L. L., and Vorburger, L. M.: Evaluation of the filter pack for long-duration sampling of ambient air, Atmos. Environ., 33, 2187–2202, https://doi.org/10.1016/S1352-2310(98)00425-7, 1999.

Simpson, D., Benedictow, A., Berge, H., Bergström, R., Emberson, L. D., Fagerli, H., Flechard, C. R., Hayman, G. D., Gauss, M., Jonson, J. E., Jenkin, M. E., Nyíri, A., Richter, C., Semeena, V. S., Tsyro, S., Tuovinen, J.-P., Valdebenito, Á., and Wind, P.: The EMEP MSC-W chemical transport model – technical description, Atmos. Chem. Phys., 12, 7825–7865, https://doi.org/10.5194/acp-12-7825-2012, 2012.

Simpson, D., Bergström, R., Imhof, H., and Wind, P.: Updates to the EMEP/MSC-W model, 2016–2017, in: Transboundary particulate matter, photo-oxidants, acidifying and eutrophying components, The Norwegian Meteorological Institute, Oslo, Norway, Status Report 1/2017, 115–122, available at: https://www.emep.int (last access: 20 May 2021), 2017.

Simpson, D., Bergström, R., Briolat, A., Imhof, H., Johansson, J., Priestley, M., and Valdebenito, A.: GenChem v1.0 – a chemical pre-processing and testing system for atmospheric modelling, Geosci. Model Dev., 13, 6447–6465, https://doi.org/10.5194/gmd-13-6447-2020, 2020.

Skamarock, W. C., Klemp, J. B., Dudhia, J., David O. Gill, D. O., Barker, D., Duda, M. G., Huang, X. Y., Wang, W., and Powers, J. G.: A Description of the Advanced Research WRF Version 3, NCAR, Tech. Note NCAR/TN-475+STR, 113 pp., https://doi.org/10.5065/D68S4MVH, 2008.

Skjøth, C. A., Geels, C., Berge, H., Gyldenkærne, S., Fagerli, H., Ellermann, T., Frohn, L. M., Christensen, J., Hansen, K. M., Hansen, K., and Hertel, O.: Spatial and temporal variations in ammonia emissions – a freely accessible model code for Europe, Atmos. Chem. Phys., 11, 5221–5236, https://doi.org/10.5194/acp-11-5221-2011, 2011.

Stadtler, S., Simpson, D., Schröder, S., Taraborrelli, D., Bott, A., and Schultz, M.: Ozone impacts of gas–aerosol uptake in global chemistry transport models, Atmos. Chem. Phys., 18, 3147–3171, https://doi.org/10.5194/acp-18-3147-2018, 2018.

Tan, J., Fu, J. S., Dentener, F., Sun, J., Emmons, L., Tilmes, S., Sudo, K., Flemming, J., Jonson, J. E., Gravel, S., Bian, H., Davila, Y., Henze, D. K., Lund, M. T., Kucsera, T., Takemura, T., and Keating, T.: Multi-model study of HTAP II on sulfur and nitrogen deposition, Atmos. Chem. Phys., 18, 6847–6866, https://doi.org/10.5194/acp-18-6847-2018, 2018.

Tang, Y. S., Braban, C. F., Dragosits, U., Dore, A. J., Simmons, I., van Dijk, N., Poskitt, J., Dos Santos Pereira, G., Keenan, P. O., Conolly, C., Vincent, K., Smith, R. I., Heal, M. R., and Sutton, M. A.: Drivers for spatial, temporal and long-term trends in atmospheric ammonia and ammonium in the UK, Atmos. Chem. Phys., 18, 705–733, https://doi.org/10.5194/acp-18-705-2018, 2018a.

Tang, Y. S., Braban, C. F., Dragosits, U., Simmons, I., Leaver, D., van Dijk, N., Poskitt, J., Thacker, S., Patel, M., Carter, H., Pereira, M. G., Keenan, P. O., Lawlor, A., Conolly, C., Vincent, K., Heal, M. R., and Sutton, M. A.: Acid gases and aerosol measurements in the UK (1999–2015): regional distributions and trends, Atmos. Chem. Phys., 18, 16293–16324, https://doi.org/10.5194/acp-18-16293-2018, 2018b.

Tang, Y. S., Flechard, C. R., Dämmgen, U., Vidic, S., Djuricic, V., Mitosinkova, M., Uggerud, H. T., Sanz, M. J., Simmons, I., Dragosits, U., Nemitz, E., Twigg, M., van Dijk, N., Fauvel, Y., Sanz, F., Ferm, M., Perrino, C., Catrambone, M., Leaver, D., Braban, C. F., Cape, J. N., Heal, M. R., and Sutton, M. A.: Pan-European rural monitoring network shows dominance of NH_3 gas and NH_4NO_3 aerosol in inorganic atmospheric pollution load, Atmos. Chem. Phys., 21, 875–914, https://doi.org/10.5194/acp-21-875-2021, 2021.

Thunis, P., Pernigotti, D., and Gerboles, M.: Model quality objectives based on measurement uncertainty. Part I: Ozone, Atmos. Environ., 79, 861–868, https://doi.org/10.1016/j.atmosenv.2013.05.018, 2013.

Tørseth, K., Aas, W., Breivik, K., Fjæraa, A. M., Fiebig, M., Hjellbrekke, A. G., Lund Myhre, C., Solberg, S., and Yttri, K. E.: Introduction to the European Monitoring and Evaluation Programme (EMEP) and observed atmospheric composition change during 1972–2009, Atmos. Chem. Phys., 12, 5447–5481, https://doi.org/10.5194/acp-12-5447-2012, 2012.

Tsyro, S., Aas, W., Soares, J., Sofiev, M., Berge, H., and Spindler, G.: Modelling of sea salt concentrations over Europe: key uncertainties and comparison with observations, Atmos. Chem. Phys., 11, 10367–10388, https://doi.org/10.5194/acp-11-10367-2011, 2011.

Vecchi, R., Valli, G., Fermo, P., D'Alessandro, A., Piazzalunga, A., and Bernardoni, V.: Organic and inorganic sampling artefacts assessment, Atmos. Environ., 43, 1713–1720, https://doi.org/10.1016/j.atmosenv.2008.12.016, 2009.

Vieno, M., Dore, A. J., Stevenson, D. S., Doherty, R., Heal, M. R., Reis, S., Hallsworth, S., Tarrason, L., Wind, P., Fowler, D., Simpson, D., and Sutton, M. A.: Modelling surface ozone during the 2003 heat-wave in the UK, Atmos. Chem. Phys., 10, 7963–7978, https://doi.org/10.5194/acp-10-7963-2010, 2010.

Vieno, M., Heal, M. R., Hallsworth, S., Famulari, D., Doherty, R. M., Dore, A. J., Tang, Y. S., Braban, C. F., Leaver, D., Sutton, M. A., and Reis, S.: The role of long-range transport and domestic emissions in determining atmospheric secondary inorganic particle concentrations across the UK, Atmos. Chem. Phys., 14, 8435–8447, https://doi.org/10.5194/acp-14-8435-2014, 2014.

Vieno, M., Heal, M. R., Williams, M. L., Carnell, E. J., Nemitz, E., Stedman, J. R., and Reis, S.: The sensitivities of emissions reductions for the mitigation of UK $PM_{2.5}$, Atmos. Chem. Phys., 16, 265–276, https://doi.org/10.5194/acp-16-265-2016, 2016.

Wagner, R., Bertozzi, B., Höpfner, M., Höhler, K., Möhler, O., Saathoff, H., and Leisner, T.: Solid Ammonium Nitrate Aerosols as Efficient Ice Nucleating Particles at Cirrus Temperatures, J. Geophys. Res.-Atmos., 125, e2019JD032248, https://doi.org/10.1029/2019JD032248, 2020.

Weiss, A. and Norman, J. M.: Partitioning solar radiation into direct and diffuse, visible and near-infrared components, Agr. Forest Meteorol., 34, 205–213, https://doi.org/10.1016/0168-1923(85)90020-6, 1985.

West, J. J., Emberson, L., Anenberg, S. C., Arnold, S., Ashmore, M., Atkinson, R., Bellouin, N., Cohen, A., Collins, B., and Delmelle, P.: Impacts on Health, Ecosystems, and Climate, in: Hemispheric Transport of Air Pollution: Part A: Ozone and Particulate Matter, Air Pollution Studies, edited by: Dentener, F., Keating, T., and Akimoto, H., United Nations, New York and Geneva, Chapter 5, 199–251, 2010.

Wiedinmyer, C., Akagi, S. K., Yokelson, R. J., Emmons, L. K., Al-Saadi, J. A., Orlando, J. J., and Soja, A. J.: The Fire INventory from NCAR (FINN): a high resolution global model to estimate the emissions from open burning, Geosci. Model Dev., 4, 625–641, https://doi.org/10.5194/gmd-4-625-2011, 2011.

Xu, L. and Penner, J. E.: Global simulations of nitrate and ammonium aerosols and their radiative effects, Atmos. Chem. Phys., 12, 9479–9504, https://doi.org/10.5194/acp-12-9479-2012, 2012.

Xu, W., Luo, X. S., Pan, Y. P., Zhang, L., Tang, A. H., Shen, J. L., Zhang, Y., Li, K. H., Wu, Q. H., Yang, D. W., Zhang, Y. Y., Xue, J., Li, W. Q., Li, Q. Q., Tang, L., Lu, S. H., Liang, T., Tong, Y. A., Liu, P., Zhang, Q., Xiong, Z. Q., Shi, X. J., Wu, L. H., Shi, W. Q., Tian, K., Zhong, X. H., Shi, K., Tang, Q. Y., Zhang, L. J., Huang, J. L., He, C. E., Kuang, F. H., Zhu, B., Liu, H., Jin, X., Xin, Y. J., Shi, X. K., Du, E. Z., Dore, A. J., Tang, S., Collett Jr., J. L., Goulding, K., Sun, Y. X., Ren, J., Zhang, F. S., and Liu, X. J.: Quantifying atmospheric nitrogen deposition through a nationwide monitoring network across China, Atmos. Chem. Phys., 15, 12345–12360, https://doi.org/10.5194/acp-15-12345-2015, 2015.

Xu, W., Zhang, L., and Liu, X.: A database of atmospheric nitrogen concentration and deposition from the nationwide monitoring network in China, Sci. Data, 6, 51, https://doi.org/10.1038/s41597-019-0061-2, 2019.

Yu, X.-Y., Lee, T., Ayres, B., Kreidenweis, S. M., Collett, J. L., and Malm, W.: Particulate Nitrate Measurement Using Nylon Filters, JAPCA J. Air Waste Ma., 55, 1100–1110, https://doi.org/10.1080/10473289.2005.10464721, 2005.

Zheng, J. Y., Yin, S. S., Kang, D. W., Che, W. W., and Zhong, L. J.: Development and uncertainty analysis of a high-resolution NH_3 emissions inventory and its implications with precipitation over the Pearl River Delta region, China, Atmos. Chem. Phys., 12, 7041–7058, https://doi.org/10.5194/acp-12-7041-2012, 2012.